Article

Remote detection of a lunar granitic batholith at Compton–Belkovich

https://doi.org/10.1038/s41586-023-06183-5

Received: 7 September 2022

Accepted: 9 May 2023

Published online: 05 July 2023

Check for updates

Matthew A. Siegler[1,2,7]✉, Jianqing Feng[1,2,7]✉, Katelyn Lehman-Franco[2], Jeffery C. Andrews-Hanna[3], Rita C. Economos[2], Michael St. Clair[4], Chase Million[4], James W. Head[5], Timothy D. Glotch[6] & Mackenzie N. White[2]

Granites are nearly absent in the Solar System outside of Earth. Achieving granitic compositions in magmatic systems requires multi-stage melting and fractionation, which also increases the concentration of radiogenic elements[1]. Abundant water and plate tectonics facilitate these processes on Earth, aiding in remelting. Although these drivers are absent on the Moon, small granite samples have been found, but details of their origin and the scale of systems they represent are unknown[2]. Here we report microwave-wavelength measurements of an anomalously hot geothermal source that is best explained by the presence of an approximately 50-kilometre-diameter granitic system below the thorium-rich farside feature known as Compton–Belkovich. Passive microwave radiometry is sensitive to the integrated thermal gradient to several wavelengths depth. The 3–37-gigahertz antenna temperatures of the Chang'e-1 and Chang'e-2 microwave instruments allow us to measure a peak heat flux of about 180 milliwatts per square metre, which is about 20 times higher than that of the average lunar highlands[3,4]. The surprising magnitude and geographic extent of this feature imply an Earth-like, evolved granitic system larger than believed possible on the Moon, especially outside of the Procellarum region[5]. Furthermore, these methods are generalizable: similar uses of passive radiometric data could vastly expand our knowledge of geothermal processes on the Moon and other planetary bodies.

Granitic rocks are common on Earth owing in part to the presence of abundant water and plate tectonics, which aid in melting and recycling crustal materials. Igneous systems elsewhere in the Solar System are dominated by basalt, representing single-stage melting of mantle rock. Granite production requires multi-stage remelting of basalt or crystal fractionation of basaltic liquids. These processes also drive an increased concentration of incompatible elements such as silicon and radiogenic potassium, thorium (Th) and uranium (U)[1]. Rare granitic clasts found in lunar samples contain a high radiogenic concentration[2]. However, the origin and scale of the systems that produced them are unknown. Lunar silicic volcanic materials, found primarily in the nearside Procellarum region[5], are generally coincident with high Th concentrations detected with orbital gamma-ray data[6–9]. Still, there is little to constrain the subsurface structures and processes that created these systems.

An enigmatic farside feature known as Compton–Belkovich[6,9] has the highest localized Th concentrations on the Moon. Located at 61.2° N, 99.7° E between its two namesake craters, the central region of Compton–Belkovich has been mapped as a likely volcanic feature and is often referred to as the Compton–Belkovich Volcanic Complex (CBVC)[10–15]. Here we present the discovery that a large granitic batholith, similar in volume to terrestrial batholiths such as the Andean Altiplano–Puna Magma Body[16] underlays Compton–Belkovich. We identify this CBVC batholith through a broad, increased local geothermal heat flux, which peaks at about 180 mW m^{-2}—approximately 20 times that of the background lunar highlands[15] and over 8 times that measured at the Apollo 15 site[16]. Such a high heat flux requires a large mid-crustal body with higher radiogenic element concentrations than previously interpreted from orbital observations[4,7]. Here we detail evidence based on a combination of models and data from the Chang'e-1 (CE-1) and Chang'e-2 (CE-2) orbiters, NASA's Lunar Reconnaissance Orbiter (LRO), and past data from the Lunar Prospector, the Gravity Recovery and Interior Laboratory (GRAIL), Chandrayaan-1 and Apollo missions.

The CE-1 and CE-2 orbiters carried four-channel (3–37 GHz) microwave radiometer (MRM) instruments. These data provide near-global coverage over most of the diurnal cycle, including 8 CE-1 and 13 CE-2 passes over the CBVC. The maps presented here are generally from CE-2, which had a lower orbit and therefore higher spatial resolution. MRM data are at antenna temperature (TA), which results from emitted brightness temperatures (Tb) as seen by the instrument field of view. Figure 1 shows the 3-GHz midnight TA in the CBVC region (after latitudinal trends have been removed and normalized to 61° N), revealing an enhancement of about 9 K, coincident with the Th anomaly. A similar 'hotspot' is observed at all frequencies, at all local times, in both CE-1 and CE-2 microwave data (Methods). We find that this Tb anomaly can only be explained by an enhanced geothermal gradient, which also

[1]Planetary Science Institute, Tucson, AZ, USA. [2]Department of Earth Sciences, Southern Methodist University, Dallas, TX, USA. [3]Department of Planetary Sciences/Lunar and Planetary Laboratory, University of Arizona, Tucson, AZ, USA. [4]Million Concepts, Louisville, KY, USA. [5]Department of Earth, Environmental and Planetary Sciences, Brown University, Providence, RI, USA. [6]Department of Geosciences, SUNY Stony Brook, Stony Brook, NY, USA. [7]These authors contributed equally: Matthew A. Siegler, Jianqing Feng. ✉e-mail: msiegler@psi.edu; jfeng@psi.edu

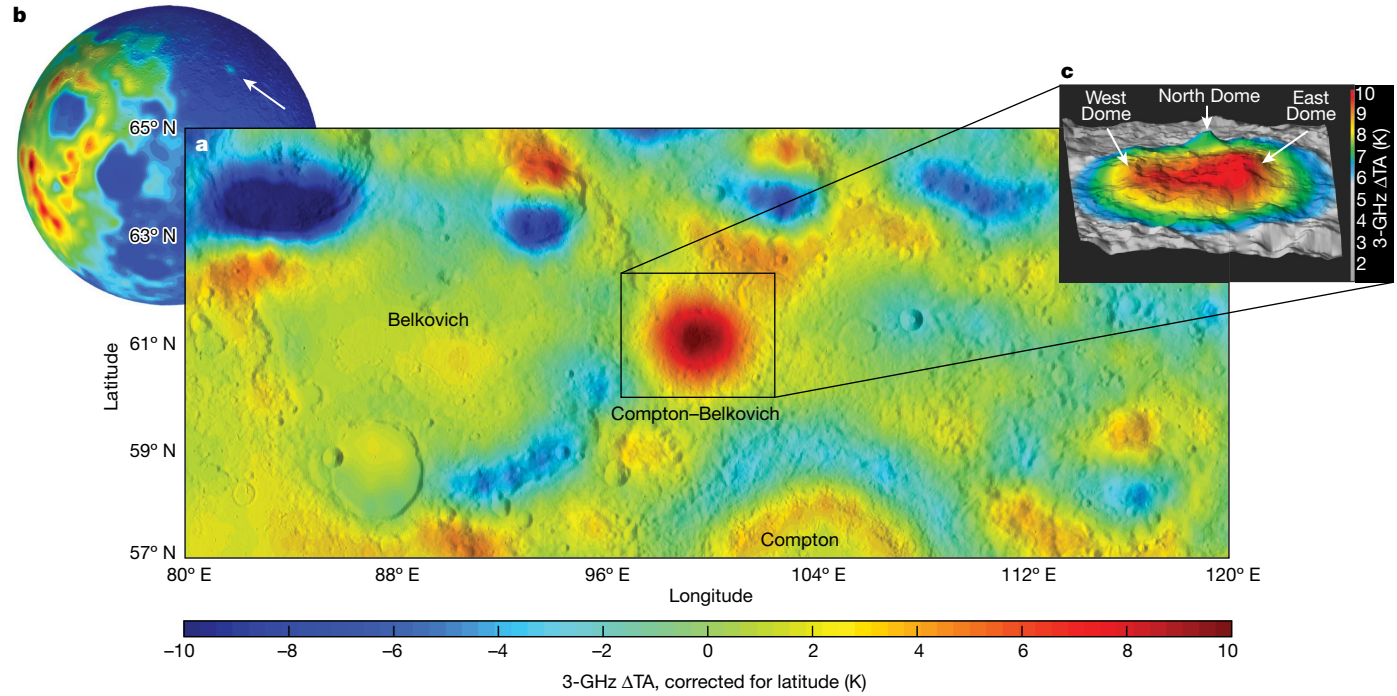

Fig. 1 | Latitudinally corrected 3-GHz TA shown at midnight local time. **a**, These data show a clear localized TA enhancement of about 9 K centred on the mapped Compton–Belkovich topographic feature. This feature is not explainable by topography, surface rock distribution or material properties and is seen at all frequencies and times of day (Methods). **b**,**c**, The context globe shows Lunar Prospector-measured Th, scaled 0–35-ppm Th (**b**) and the perspective view shows the TA superimposed on the central CBVC caldera topography (**c**).

provides a technique that could provide a window into the interior compositions of the Moon and other planetary bodies.

The CBVC consists of a central, aproximately 15-km-diameter plain ringed by 3-km-scale domes[8–12]. The high-albedo interior shows a short-wavelength infrared Christiansen feature consistent with a silicic surface[8], and photometric detections of minerals andesite and dacite[11], which is proposed evidence of erupted rhyolitic lavas[8–12]. Interior to the domes, several groups have mapped what appear to be circumferential faulting suggestive of a piston-style collapsed caldera[10,12]. These features have been hypothesized to mark the edge of a once-inflated magma body, potentially now evacuated, approximately 13 km in diameter. The greater region surrounding the CBVC shows an enhanced Th concentration, postulated to be an ashfall deposit[9], leading to estimates of erupted materials' volume and plausible water content[17]. However, previous studies have been limited to studying the surface signature of the volcanism, making indirect inferences regarding what lies beneath.

Microwave radiometry provides a means to peer below the surface to measure the integrated subsurface physical temperature. The measurement frequency and the dielectric properties (summarized by the loss tangent, which is the ratio between the real and imaginary dielectric constants)[18,19] controls the depth over which materials add to the emitted radiance. Lower frequencies (longer wavelengths) and lower loss tangents will sense heat from greater depths. Conversely, higher frequencies and higher loss tangents will sense temperatures closer to the surface. For MRM frequencies and lunar materials, sounding depths are estimated at about 0.3 m to 5.6 m (ref. 19).

On Earth, water's high dielectric loss limits microwave penetration. The Moon, Mars and other planetary bodies with dry conditions, regolith cover and low atmospheric pressure exhibit extremely low loss tangents (<0.01), enabling microwave remote sensing to greater depths. Furthermore, the low thermal conductivity of the lunar regolith ($<10^{-3}$ W m^{-1} K^{-1}) both shows diurnal temperature variations (to the upper approximately 50 cm) and provides high geothermal gradients (>1 K m^{-1})[4]. Consequently, increases in temperature with depth owing to the geothermal gradient will increase measurable brightness temperatures, with a stronger signal at lower frequencies. Figure 2 illustrates the relationship between the modelled gradient from various geothermal fluxes (Fig. 2a), the weighting function over which emitted heat is integrated for each Chang'e frequency (Fig. 2b) and the resulting increase in relative brightness temperature as a function of heat flux (Fig. 2c).

We find no plausible explanation for the high TAs other than an enhanced subsurface geothermal heat source. Low albedo can cause higher Tb, but the CBVC has a higher albedo than its surroundings. Changes in near-surface density or loss tangent will alter the diurnal Tb amplitude[19], but higher Tb are seen at all local times. We find the CBVC feature is similar in near-surface density and loss to the surrounding region, with a loss tangent of about 0.005–0.01 (Methods). With these losses, 3-GHz measurements should be sensitive to heat within the upper approximately 5.5 m (ref. 19).

The TA obtained by a microwave radiometer depends on the instrument radiation pattern (the angular dependence of power density). Using a multi-frequency fit at two altitudes (about 200 km for CE-1 and about 100 km for CE-2) and instrument antenna patterns (Methods), we can use the variable resolution to characterize the magnitude, size and shape of the heat source. First, we create a forward model of subsurface emission from solar heating, fit to LRO Diviner infrared measurements accounting for effects of slope, azimuth, density, LRO Diviner rock abundance and loss tangents fit from Chang'e data (Methods). Then we apply a frequency-dependent antenna pattern to the forward model of the emitted microwave radiance, converting from modelled Tb to TA. The resulting TA models provide a good fit for temperature variations owing to topography and surface geology, but reveal a strong Tb excess in both CE-1 and CE-2 data at the CBVC (Methods), seen at all frequencies (Fig. 3).

Although this enhancement's location coincides with the increased surface Th observed at the CBVC[7,9], it is a much larger increase than explainable by surface materials. Previous orbital measurements estimate CBVC to have up to about 26-ppm Th (ref. 9), within the range

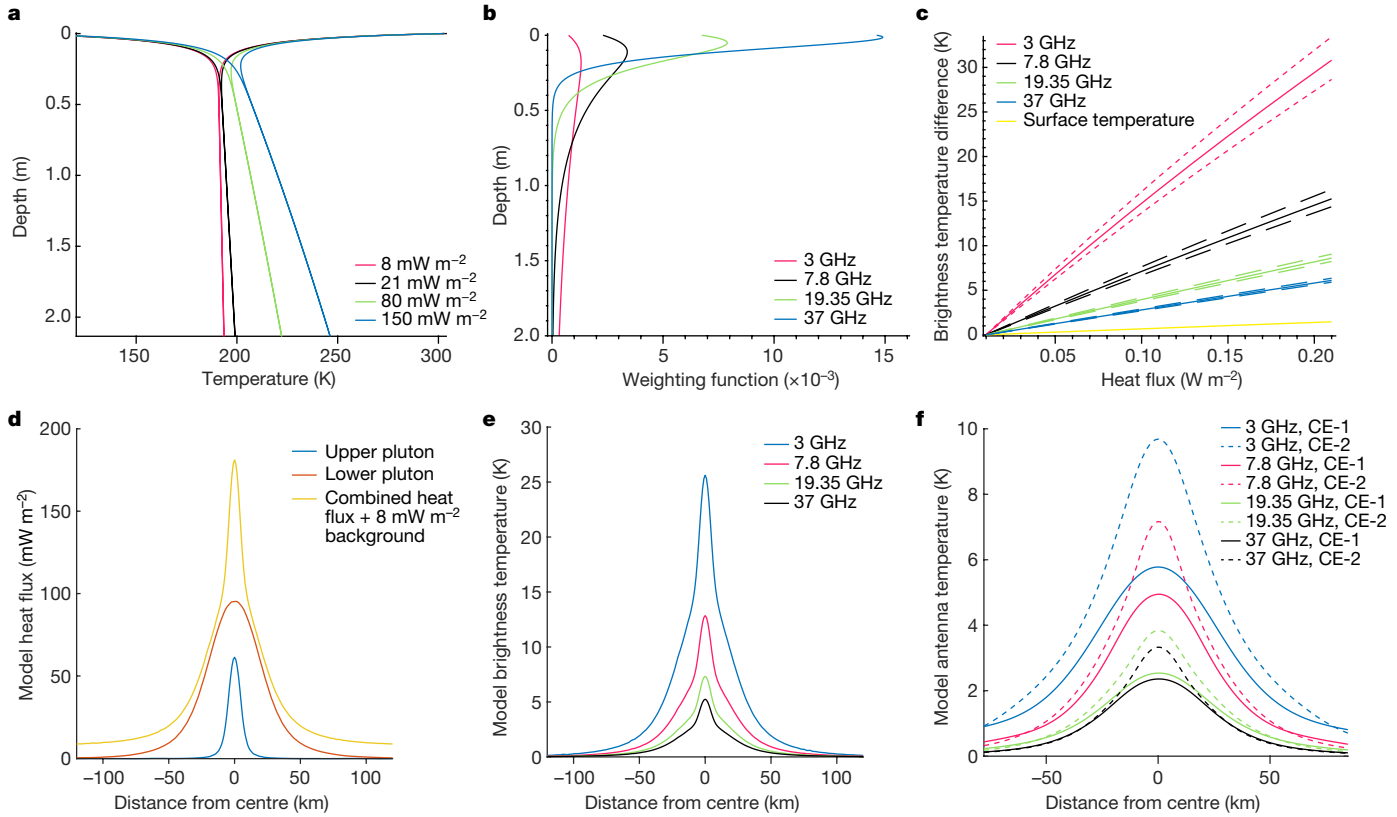

Fig. 2 | Microwave expectations from a geothermal source. a, Physical temperature versus depth for the CBVC location for various geothermal fluxes. **b**, The CE-1 and CE-2 MRM weighting functions in highlands regolith. **c**, The ΔTb for a given heat flux. The dashed lines represent ±10% variation in loss tangent. **d**, The heat flux from our nominal two-pluton model (orange) resulting from the combined upper (blue) and lower (red) pluton contributions with 8 mW m^{-2} background heat flux. **e**, The resulting ΔTb for each measurement for our end-member two-pluton model. **f**, The resulting ΔTA for each measurement for our end-member two-pluton model.

of lunar granitic samples[18]. A heat flux of 180 mW m^{-2} would require a layer of roughly 45 km of such material, neglecting any lateral heat conduction, implying the material below the surface exceeds concentrations estimated at the surface. In reality, heat will spread into the surrounding crust, so 26-ppm Th would require an even thicker deposit, exceeding the approximately 50-km crustal column in this location[20]. This lateral spread of heat flux helps define the size and depth of the heat source, as a wider or deeper source would increase the spread by the conduction of heat through the crust. Although there is a trade-off between the source depth, size and radiogenic element concentration, we can provide bounds by examining remote sensing, samples and petrologic data. On the basis of returned igneous lunar

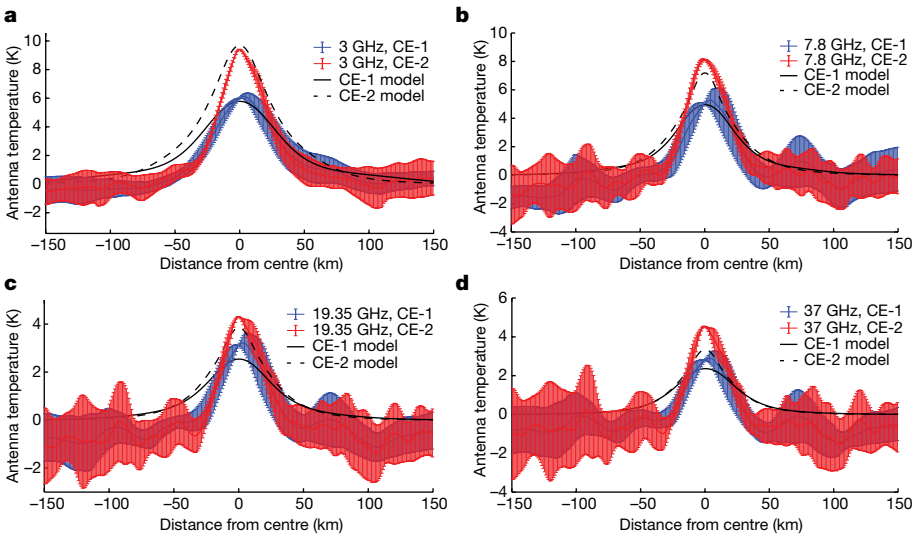

Fig. 3 | Data minus forward model TA compared with the best-fit pluton model. a–**d**, The 3-GHz (**a**), 7.8-GHz (**b**), 19.35-GHz (**c**) and 37-GHz (**d**) CE-1 and CE-2 residual ΔTA data-model as a function of distance from the centre of the CBVC. Negative and positive values are averages in radial distance from the centre of the CBVC with 1σ error for all data westwards and eastwards of the feature, respectively. A clear spike is seen at all frequencies as mapped in Fig. 1 and Methods. The input model heat flux values are from Fig. 2d, and Fig. 2e,f shows how these ΔTA values result from the heat flux inputs.

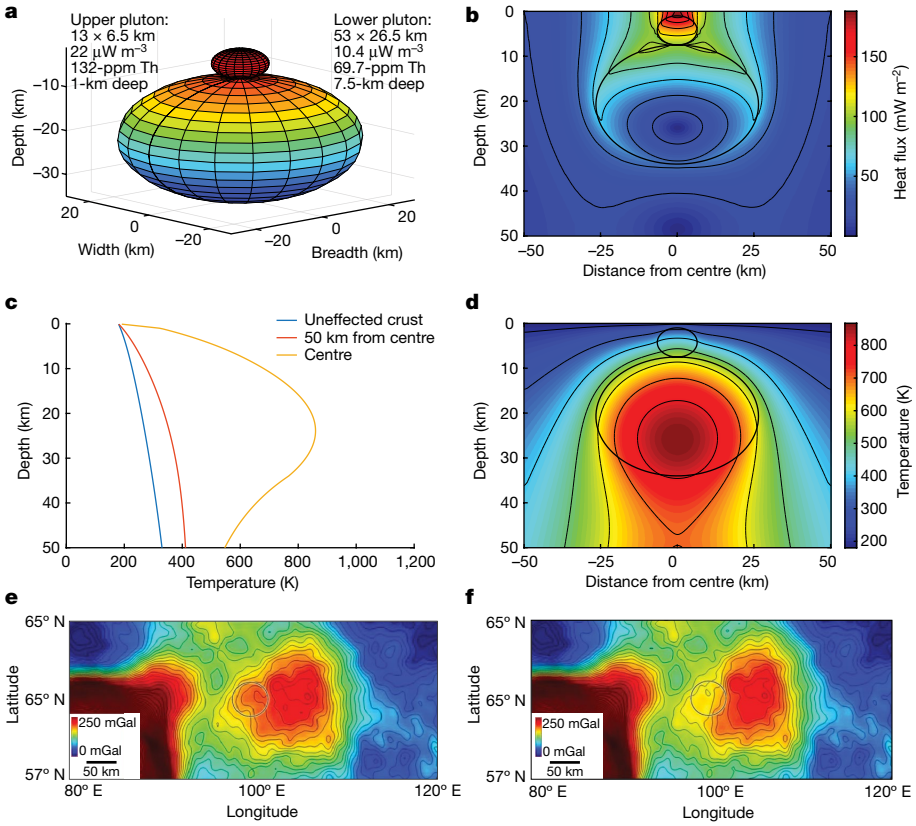

Fig. 4 | Geophysical models of the Compton–Belkovich batholith. a,**b**, Our end-member Compton–Belkovich pluton model based on fitting of the surface heat flux enhancement (**a**) and the resulting heat flux (**b**). **c**,**d**, The subsurface temperatures predicted by this model as a function of depth (**c**) and cross section (**d**). **e**,**f**, GRAIL Bouguer gravity (in units of mGal) of the CBVC region (**e**) and GRAIL Bouguer gravity after removing the gravity signature of a model from the middle of our preferred range (**f**; 90 kg m^{-3} density anomaly for the lower body). The CBVC gravity anomaly associated with this pluton sits on the shoulder (small circle) of a broader and higher magnitude anomaly associated with the larger Compton–Belkovich region.

samples, only quartz monzodiorite, felsite and granite samples have higher than 26-ppm Th.

The evidence of Th-rich silicic volcanism from remote sensing, geomorphology, and Th-rich granites and quartz monzodiorites within the Apollo samples lead to a reasonable assertion that the CBVC may be underlain by a granitic body[8,12–15]. Therefore, we attempt to fit the residual TA increase with a forwards model of a discrete subsurface geothermal heat source assuming a geometry of an elliptical pluton. We give crustal material outside the CBVC commonly assumed heat production values[21], resulting in a surface flux of about 8 mW m^{-2}. To match the observed Tb and geometry, we begin with a 13-km-wide ellipsoidal body at 1-km depth. To provide a peak heat flux of 180 mW m^{-2} on the surface would require about 60 × 10^{-6} W m^{-3} of heat production. However, this is about 3 times the heat production of the most radiogenic materials found in lunar samples[22], equivalent to about 400-ppm Th, which is highly unlikely. To examine reasonable source materials, we look to high-Th Apollo lunar samples: these fall into three classes; 35–44-ppm Th quartz monzodiorites (here labelled G_A)[23,24], about 62–70-ppm Th granites (G_B)[22,23,25] and a single, highly evolved Apollo 12 granite sample with 132-ppm Th (G_C)[25].

Modelling the upper body as G_C composition can serve as an end-member case, but itself is probably unreasonably high. Even with this high radiogenic concentration, a 13-km body will not produce enough heat (it results in the blue heat flux curve in Fig. 2d). Therefore, we conclude that the CBVC underlain by a deeper, much larger and probably less radiogenic body. Such a large, second body is also a sensible geologic assumption as it would provide a lower-Th, intermediate-stage reservoir from which to distil the upper pluton. In reality, the lower body is probably composed of several intermediate chambers and sills (Methods), with this ellipsoidal shape approximating their net heat production and gravity.

With this simplified geometry (assuming 2:1 ellipsoid aspect ratios), we tested approximately 600 model variations in upper and lower pluton sizes. For 10–20-km-diameter upper plutons, solutions for the lower body fall within a narrow trade space, with diameters of 47 km and 57 km (Methods). Our end-member model retains the upper G_C pluton as 13 km in diameter at 1-km depth, which will minimize the volume of the lower body, providing a lower limit for its size. We obtain a best-fit surface heat flux for a lower body with G_B concentration at about 53 km in diameter at about 7.5-km depth (centred at 20.5-km depth; Methods). The resulting heat flux peaks at 180 mW m^{-2}, making this the highest detected heat flux on the Moon, approximately 20 times the 5–10 mW m^{-2} highlands background[3]. Figure 2d shows our end-member model heat flux (in orange, with the heat for the upper and lower pluton shown in blue and red), Fig. 2e shows the resulting Tb at each frequency and Fig. 2f shows the resulting TA for the two antenna models. Figure 3 shows the same curves in Fig. 2f compared with the Chang'e data as a function of distance from the centre of the CBVC. The two bodies in this end-member model represent up to 1.7% of the total lunar Th budget estimated from surface concentrations[3]. This is not unique, and this model depends on assumed radiogenic concentrations and pluton shapes, but serves as a first-order model. A model assuming no heat production from the upper pluton results in a poor fit, but results in a lower body that is still under 60 km in diameter, providing an upper limit on the size of Compton–Belkovich batholith (assuming G_B composition; Methods).

Figure 4 illustrates the resulting temperature and heat flux from our end-member modelled pluton. In Fig. 4b–d, we find a peak temperature

of 867 K within the lower pluton, placing it below the liquidus at present, but feasibly molten in the past. Heat sources assuming quartz monzodiorite (G_A composition) required bodies the scale of the entire 50-km crustal column and would result in a much wider surface expression. Deeper, larger G_B concentration bodies also produce a more laterally extensive surface heat flux than is consistent with the data, again requiring a mid-crustal heat source. This heat flux could warm nighttime surface temperatures by about 1 K, but we cannot detect this signal among effects of local topography and albedo in LRO Diviner data (Methods).

GRAIL Bouguer gravity data reveal a narrow positive gravity anomaly centred on and comparable in scale to the microwave brightness anomaly on the shoulder of the broader Compton–Belkovich region Bouguer gravity high. Although it is impossible to uniquely constrain the density structure owing to the large regional gravity anomalies, we can test whether the end-member pluton model is consistent with the observed gravity. The modelled gravity arising from this pluton model matches the observed anomaly for density contrasts of the lower body ranging from 60 kg m^{-3} to 120 kg m^{-3} relative to the surroundings, with the density anomaly of the upper body assumed to be half that of the lower body. These density contrasts equate to absolute densities of 2,940–3,000 kg m^{-3} and 2,470–2,500 kg m^{-3} for the lower and upper bodies, respectively, based on a linear density model for the farside highlands[26]. Assuming a low porosity, the density of the lower body implies a material that is somewhat less dense than typical mare[27], consistent with a slightly more silicic composition, whereas the low density of the upper body suggests a more evolved and silicic intrusion. Figure 4e,f shows the effect of removing the gravity anomaly from a model assuming a 90 kg m^{-3} density anomaly for the lower batholith from the observed gravity.

These data solidify the conclusion that Compton–Belkovich is the result of felsic volcanism and provide evidence for an evolved magma plumbing system much larger than expected on the Moon[1,5,8,9,15,28]. A magmatic system of this size requires one of the following features: (1) a long-lived thermal source, such as a farside mantle plume (which appears in some models[29]), to facilitate multi-stage magmatic processing; (2) an anomalously wet pocket of the otherwise dry Moon (consistent with CBVC volcanic estimates of 2 wt% water[17]), which could lower the local melting point; or (3) a farside KREEP (potassium (K), rare-earth elements (REE) and phosphorus (P) rich) layer that could build sufficient radiogenic material to remelt through self-heating. All scenarios imply large-scale compositional heterogeneities in the mantle and/or crust during lunar formation.

Petrogenesis of lunar granites, felsites and quartz monzodiorites is subject to ongoing debate centred around four models: (1) differentiation driven by silicate–iron liquid immiscibility[30,31]; (2) remelting of lunar crust in large impact events[32]; (3) crystal fractionation of KREEP basaltic liquids[33–35]; and (4) partial melting of KREEP-rich monzogabbro and alkali gabbronorite crust[8,36]. Hypothesis 1 is precluded at the CBVC owing to the large volume needed as well as lack of correlation between high Th contents and a large positive Bouguer gravity anomaly, as Th would fractionate into the denser, iron-rich component[36]. The system's geometry required to accommodate the observed heat-flow anomalies precludes hypothesis 2. Thus, both remaining scenarios, or probably a combination of the two, require the initial presence of a farside KREEP component to form the CBVC system. The distillation of radiogenic elements via remelting or crystal fractionation from KREEP components is needed to achieve the U and Th compositions that produce the observed heat-flow feature. The KREEP-rich material beneath Compton–Belkovich may represent a local thickening of a former continuous farside KREEP layer or a relict patch of KREEP left behind after a global layer was remobilized to the nearside[37,38].

Furthermore, this work illustrates a new tool for mapping a planetary geothermal gradient from orbit through passive microwave radiometry, which can provide a window into crustal and interior heat-producing structures. The high heat flux and relatively low-loss material at Compton–Belkovich allowed the multiple short wavelengths of the Chang'e instruments to uniquely constrain the geothermal flux. Longer wavelengths will be required to map the lower heat flux seen over most of the Moon and other bodies, highlighting a path forwards in future spacecraft instrumentation. Such data should be ground-truthed on the Moon by a globally distributed heat flux network[17,39]. Techniques such as in situ heat flux, seismic, electromagnetic, long-wavelength radar exploration and sample geochemical analysis could further characterize the presence, size and origin of the Compton–Belkovich pluton system. Our results conclude that this is a highly evolved, multi-stage, batholith-scale, granitic magmatic system—a phenomenon previously documented only on Earth.

Online content

Any methods, additional references, Nature Portfolio reporting summaries, source data, extended data, supplementary information, acknowledgements, peer review information; details of author contributions and competing interests; and statements of data and code availability are available at https://doi.org/10.1038/s41586-023-06183-5.

1. Pitcher, W. S. *The Nature and Origin of Granite* (Springer Science & Business Media, 1997).
2. Seddio, S. M., Korotev, R. L., Jolliff, B. L. & Wang, A. Silica polymorphs in lunar granite: implications for granite petrogenesis on the Moon. *Am. Mineral.* **100**, 1533–1543 (2015).
3. Siegler, M. A. et al. Lunar heat flow: global predictions and reduced heat flux. *J. Geophys. Res. Planets* https://doi.org/10.1029/2022JE007182 (2022).
4. Langseth, M. G., Keihm, S. J. & Peters, K. Revised lunar heat-flow values. In *Proc. Lunar and Planetary Science Conference* Vol. 7, 3143–3171 (Lunar and Planetary Institute, 1976).
5. Glotch, T. D. et al. Highly silicic compositions on the Moon. *Science* **329**, 1510–1513 (2010).
6. Lawrence, D. J. et al. High resolution measurements of absolute thorium abundances on the lunar surface. *Geophys. Res. Lett.* **26**, 2681–2684 (1999).
7. Lawrence, D. J. et al. Small-area thorium features on the lunar surface. *J. Geophys. Res. Planets* https://doi.org/10.1029/2003JE002050 (2003).
8. Hagerty, J. J. et al. Refined thorium abundances for lunar red spots: Implications for evolved, nonmare volcanism on the Moon. *J. Geophys. Res. Planets* https://doi.org/10.1029/2005JE002592 (2006).
9. Wilson, J. T. et al. Evidence for explosive silicic volcanism on the Moon from the extended distribution of thorium near the Compton–Belkovich Volcanic Complex. *J. Geophys. Res. Planets* **120**, 92–108 (2015).
10. Jolliff, B. L. et al. Compton–Belkovich: nonmare, silicic volcanism on the Moon's far side. In *Proc. 42nd Annual Lunar and Planetary Science Conference* 1608, 2224 (Lunar and Planetary Institute, 2011).
11. Jolliff, B. L. et al. Non-mare silicic volcanism on the lunar farside at Compton–Belkovich. *Nat. Geosci.* **4**, 566–571 (2011b).
12. Jolliff, B. L. et al. Compton–Belkovich Volcanic Complex. In *Proc. Lunar and Planetary Science Conference* 1659, 2097 (Lunar and Planetary Institute, 2012).
13. Clegg-Watkins, R. N. et al. Nonmare volcanism on the Moon: photometric evidence for the presence of evolved silicic materials. *Icarus* **285**, 169–184 (2017).
14. Chauhan, M., Bhattacharya, S., Saran, S., Chauhan, P. & Dagar, A. Compton–Belkovich Volcanic Complex (CBVC): an ash flow caldera on the Moon. *Icarus* **253**, 115–129 (2015).
15. Head, J. W. & Wilson, L. Generation, ascent and eruption of magma on the Moon: new insights into source depths, magma supply, intrusions and effusive/explosive eruptions (part 2: predicted emplacement processes and observation). *Icarus* **283**, 176–223 (2017).
16. del Potro, R., Díez, M., Blundy, J., Camacho, A. G. & Gottsmann, J. Diapiric ascent of silicic magma beneath the Bolivian Altiplano. *Geophys. Res. Lett.* **40**, 2044–2048 (2013).
17. Wilson, L. & Head, J. W. Explosive volcanism associated with the silicic Compton–Belkovich volcanic complex: implications for magma water content. In *Proc. 47th Lunar and Planetary Science Conference* 1564 (Lunar and Planetary Institute, 2016).
18. Feng, J., Siegler, M. A. & Hayne, P. O. New constraints on thermal and dielectric properties of lunar regolith from LRO diviner and CE-2 microwave radiometer. *J. Geophys. Res. Planets* https://doi.org/10.1029/2019JE006130 (2020).
19. Siegler, M. A. et al. Lunar titanium and frequency-dependent microwave loss tangent as constrained by the Chang'e-2 MRM and LRO diviner lunar radiometers. *J. Geophys. Res. Planets* https://doi.org/10.1029/2020JE006405 (2020).
20. Wieczorek, M. A. et al. The crust of the Moon as seen by GRAIL. *Science* **339**, 671–675 (2013).
21. Siegler, M. A. & Smrekar, S. E. Lunar heat flow: regional prospective of the Apollo landing sites. *J. Geophys. Res. Planets* **119**, 47–63 (2014).
22. Seddio, S. M., Jolliff, B. L., Korotev, R. L. & Carpenter, P. K. Thorite in an Apollo 12 granite fragment and age determination using the electron microprobe. *Geochim. Cosmochim. Acta* **135**, 307–320 (2014).
23. Ryder, G. & Martinez, R. R. Evolved hypabyssal rocks from station 7, Apennine Front, Apollo 15. In *Proc. Lunar and Planetary Science* Vol. 21, 749 (Lunar and Planetary Institute, 1991).
24. Warren, P. H., Taylor, G. J. & Keil, K. Regolith breccia Allan Hills A81005: evidence of lunar origin, and petrography of pristine and nonpristine clasts. *Geophys. Res. Lett.* **10**, 779–782 (1983).
25. Seddio, S. M., Jolliff, B. L., Korotev, R. L. & Zeigler, R. A. Petrology and geochemistry of lunar granite 12032, 366-19 and implications for lunar granite petrogenesis. *Am. Mineral.* **98**, 1697–1713 (2013).

26. Goossens, S. et al. High-resolution gravity field models from GRAIL data and implications for models of the density structure of the Moon's crust. *J. Geophys. Res. Planets* **125**, e2019JE006086 (2020).
27. Kiefer, W. S., Macke, R. J., Britt, D. T., Irving, A. J. & Consolmagno, G. J. The density and porosity of lunar rocks. *Geophys. Res. Lett.* **39**, L07201 (2012).
28. Gillis, J. J. et al. The Compton–Belkovich region of the Moon: remotely sensed observations and lunar sample association. In *Proc. Lunar and Planetary Science Conference* (Lunar and Planetary Institute, 2002).
29. Laneuville, M. et al. A long-lived lunar dynamo powered by core crystallization. *Earth Planet. Sci. Lett.* **401**, 251–260 (2014).
30. Neal, C. R. & Taylor, L. A. The nature and barium partitioning between immiscible melts—a comparison of experimental and natural systems with reference to lunar granite petrogenesis. In *Proc. Lunar and Planetary Science Conference* Vol. 19, 209–218 (Lunar and Planetary Institute, 1989).
31. Fagan, T. J., Kashima, D., Wakabayashi, Y. & Suginohara, A. Case study of magmatic differentiation trends on the Moon based on lunar meteorite Northwest Africa 773 and comparison with Apollo 15 quartz monzodiorite. *Geochim. Cosmochim. Acta* **133**, 97–127 (2014).
32. Rutherford, M. J., Hess, P. C., Ryerson, F. J., Campbell, H. W. & Dick, P. A. The chemistry, origin and petrogenetic implications of lunar granite and monzonite. In *Proc. Lunar and Planetary Science Conference* Vol. 7, 1723–1740 (Lunar and Planetary Institute, 1976).
33. Ryder, G., Stoeser, D. B., Marvin, U. B. & Bower, J. F. Lunar granites with unique ternary feldspars. In *Proc. Lunar and Planetary Science Conference* Vol. 6, 435–449 (Lunar and Planetary Institute, 1975).
34. Hess, P. C., Horzempa, P. & Rutherford, M. J. Fractionation of Apollo 15 KREEP basalts. In *Proc. Lunar and Planetary Science Conference* Vol. 20 (Lunar and Planetary Institute, 1989).
35. Marvin, U. B., Lindstrom, M. M., Holmberg, B. B. & Martinez, R. R. New observations on the quartz monzodiorite-granite suite. In *Proc. Lunar and Planetary Science Conference* Vol. 21, 119–135 (Lunar and Planetary Institute, 1991).
36. Gullikson, A. L., Hagerty, J. J., Reid, M. R., Rapp, J. F. & Draper, D. S. Silicic lunar volcanism: testing the crustal melting model. *Am. Mineral.* **101**, 2312–2321 (2016).
37. Warren, P. H. & Wasson, J. T. The origin of KREEP. *Rev. Geophys.* **17**, 73–88 (1979).
38. Taylor, S. R. & McLennan, S. *Planetary Crusts: Their Composition, Origin and Evolution* Vol. 10 (Cambridge Univ. Press., 2009); https://doi.org/10.1017/CBO9780511575358.
39. Neal, C. R. et al. The Lunar Geophysical Network (LGN) is critical for Solar System science and human exploration. In *Proc. Lunar and Planetary Science Conference* 2355 (Lunar and Planetary Institute, 2020).

Methods

Instrument background and loss tangent maps

The MRM instruments carried by CE-1 and CE-2 made measurements in four spectral channels (3.0 GHz, 7.8 GHz, 19.35 GHz and 37 GHz)[40]. The CE-1 data have channel-dependent resolutions of about 35–50 km from its orbital altitude of about 200 km, whereas the CE-2 data have resolutions of about 17.5–25 km because its orbital altitude was about 100 km. The microwave observations have been used to estimate regolith thickness[41], dielectric properties[18,19,42], rock abundance[43,44], subsurface temperatures[45] and geothermal heat flow[46,47] as well as the eruption phase of basaltic volcanism in the mare of the Moon[48]. In the polar region, MRM data analysis usually focuses on searching for evidence of water ice[49] and studying the thermal gradient[50].

A quantity known as the dielectric loss tangent, tan δ, controls the depth from which microwave energy is emitted. This is simply the ratio between the real, ε', and imaginary, ε'', dielectric constants, with $\tan\delta = \varepsilon''/\varepsilon'$. Extended Data Fig. 1 shows the mapped 'integrated loss tangent', or average loss tangent over the depth sounded by a given frequency as described in ref. 19. These maps are based on diurnal microwave amplitudes, increasing with higher loss as soundings are closer to the surface. Diurnal amplitudes are fit using all data within a 1/4° box of each point. As discussed in refs. 18,19, there appear to be substantial offsets in the absolute temperature calibration of the Chang'e data, but the relative calibration (comparing location to location or diurnal amplitudes) appears robust and in alignment with model expectations. All work in this paper relies on relative calibration (for example, how hot Compton–Belkovich is compared with its surroundings at a given frequency). The striping in Extended Data Fig. 1 is owing to variable time of day coverage in producing a fit to the diurnal amplitude.

From these maps, we argue that there is no loss anomaly associated with the Compton–Belkovich feature that could explain the enhanced TA. Features such as Dugan J (the small, fresh crater directly to the east of CBVC) or Compton crater (the large crater at about 57° N, 104° E) have a higher loss. The apparent low-loss areas on high-latitude craters result from low amplitudes owing to topographic shadowing not accounted for in these fits. Extended Data Fig. 1 illustrates the average integrated loss tangent for CBVC (black) and the entire map in Extended Data Fig. 1 (red) compared with the highlands terrain model from ref. 19 (blue line). However, a high loss would decrease the apparent heat flux, not increase it—making our heat flux estimates a lower limit.

On this basis, we use the Extended Data Fig. 1 loss tangent maps to derive appropriate microwave weighting functions, w, which relates the physical temperature versus depth, $T(z)$, to the microwave Tb at a given frequency under nadir observation as $T_b = \int_0^\infty w(z)T(z)\mathrm{d}z$. The discrete form is $T_b = \sum_{i=1}^{n} w_i T_i$, where n is the total number of layers. T_i is the physical temperature of layer i and w_i is the effective weighting function, which has been convolved with thickness d_i. In a non-scattering medium based on refs. 51,52, w_i can be expressed as:

$$w_i = (1-\Gamma)(1-\mathrm{e}^{-\kappa_i d_i})(1+|R_{i(i+1)}|^2 \times \mathrm{e}^{-\kappa_i d_i}) \times \prod_{j=1}^{i} ((1-|R_{j(j+1)}|^2)\mathrm{e}^{-\kappa_j d_j}) \quad (1)$$

where Γ is the surface reflectivity and κ_i is the power absorption coefficient of layer i, d_i is the layer thickness and $R_{i(i+1)}$ is the reflection coefficient between layer i and layer $i+1$, and j represents the layers between i and the surface within the product integration, $\prod$. For nadir observations (no off-nadir data is used in this paper), $R_{i(i+1)}$ is given from the real dielectric constant of the layer such that:

$$R_{i(i+1)} = \frac{\sqrt{\varepsilon'_{i+1}} - \sqrt{\varepsilon'_i}}{\sqrt{\varepsilon'_{i+1}} + \sqrt{\varepsilon'_i}} \quad (2)$$

the power absorption coefficient, κ_i, is given by:

$$\kappa_i = 2\frac{2\pi f}{c}\left(\frac{\varepsilon'}{2}(\sqrt{1+\tan^2\delta}-1)\right)^{1/2} \quad (3)$$

where f is the frequency, c is the speed of light, ε' is the real dielectric constant (which we set as 1.92^{ρ} (ref. 53), for density, ρ) and tan δ is the loss tangent. κ_i determines the penetration depth of microwave radiation. As physical temperature amplitudes decrease with depth and loss changes the depth being sensed, the diurnal amplitude of T_b can be used to calculate the κ_i and dielectric loss (see details in refs. 18,19).

Antenna model

The model TA results from a convolution of the emitted Tb from the Moon and the instrument antenna pattern. During the ground calibration test for the CE-1 system, the antenna patterns of the four channels were measured[54]. In this study, we fitted the antenna pattern of four channels in a Gaussian form based on published parameters. These parameters provided constraints on the main beam and the 3-dB efficiency and beam width. As the main lobe contributes >68% of the total signal at all frequencies[54], we consider only the main lobe and the first side lobes, which are treated as secondary Gaussians. CE-1 MRM and CE-2 MRM are almost identical, so the same angular antenna radiation pattern is used for both datasets. Extended Data Fig. 2 gives the modelled antenna patterns of four frequencies. For simplicity, we have assumed symmetric antenna patterns, but in reality, there are small differences in the E and H plane beam width.

This multi-frequency, multi-altitude fit allows for the constraint of a unique source function of the emitted heat from the surface. These patterns result in a different area in the instrument footprint filled with the CBVC heat source at each frequency. For example, the spatial footprint (generally defined by the 3-dB values) is approximately 25 km for CE-2 at 3 GHz and 17.5 km for the remaining channels. For CE-1 (approximately at twice the orbital altitude), this is 50 km and 35 km, respectively. This will cause a smearing of any heat source that is dependent on frequency and altitude.

As discussed in the following section, we perform some simple processing of the Chang'e data, such as latitude correction. We do not otherwise change the data from the available TA values in the Chang'e archive (included in the supplementary data) for effects such as footprint resolution, but instead process only our forward model of Tb to create a model TA. Also, as discussed in the following section, we use our antenna pattern and a thermal model for the CBVC region to produce a forward model of the TA that should be observed from solar heating alone. We then can subtract this from the data to create a map of TA that is ideally solely from increases in geothermal heat. We then produce forward models of geothermal heating from our pluton models (Extended Data Fig. 3) to produce a map of surface heat flux. Cross-sections of our end-member model heat flux are shown in Fig. 2d. We then convert this to a Tb signal (Fig. 2e) including a convolution with the antenna pattern for a given frequency, with the resulting TA as shown in Figs. 2f and 3.

As shown in Fig. 2c, there is an approximately linear relationship between the Tb and the geothermal gradient at any given frequency. For the highlands average loss tangent[19], this relationship follows as (for a heat source, HF, in units of W m^{-2}):

Tb_3G = $-89.24 \times \mathrm{HF}^2 + 166.2 \times \mathrm{HF} - 1.294$

Tb_7.8G = $-24.23 \times \mathrm{HF}^2 + 79.14 \times \mathrm{HF} - 0.6259$

Tb_19G = $-8.118 \times \mathrm{HF}^2 + 43.94 \times \mathrm{HF} - 0.3494$

Tb_37G = $-4.520 \times \mathrm{HF}^2 + 31.17 \times \mathrm{HF} - 0.2482$

Ten-percent changes in the loss tangent will result in fits plotted as dashed lines in Fig. 2c. This relationship assumes a background heat flux of 8 mW m^{-2}, which was a reasonable expectation for this region based on the crustal heat production models shown in Fig. 4.

We then perform some straightforward processing of the Chang'e data, such as latitude correction, as discussed in the following sections.

Also as discussed in the following section, we use our antenna pattern and a thermal model for the CBVC region to produce a forward model of the TA that should be observed from solar heating alone. We then can subtract this from the data to produce a map of TA that is ideally solely from increases in geothermal heat. Finally, we plot the TA models from geothermal heating (from Fig. 2d–f) against the data (corrected for latitude) in Fig. 3.

Data processing

To produce mapped values of microwave Tb, we interpolated the raw data points of MRM measurements into gridded data map. This is the same process used in refs. 18,19 and produces approximately 1/4°-resolution maps for the CE-2 MRM data. These data are shown in a time series in Extended Data Fig. 3a, which shows that the CBVC is hotter than the surroundings at all local times at all frequencies. These data are shown as a noontime map in Extended Data Fig. 3b. These maps highlight the CBVC hotspot, but it is not necessarily larger than variations owing to topography. We then remove topographic effects with models of the effects of solar illumination. CE-1 data will produce a similar map at lower resolution with a less apparent rise at the CBVC. We should note here that the absolute values of these Tb are not a clear match to model expectations given the currently available calibration of the Chang'e MRM data. This has been noted in many publications and discussed in detail in refs. 18,19. However, relative changes in Tb are well within line of model expectations. The relative point-to-point data comparison we rely on here (CBVC is hotter than the adjacent area) is quite robust.

Taking advantage of the well calibrated relative Tb variations, or ΔTb, we can have confidence in maps removing average trends for a given latitude, albedo, slope, loss tangent and so on. The simplest of those corrections is to remove the Tb trend as a function of latitude. For this 'correction', we simply take and longitudinal average over data from a relatively crater-poor section of the data (104–112° longitude) in Extended Data Fig. 3b, then smooth it (averaged over 200 pixels, or about 1° latitude) to obtain a roughly linear trend as a function of latitude. Extended Data Fig. 3c illustrates how this correction alone makes clear the abnormality of the CBVC site. This is most apparent in the 3-GHz data, showing the largest relative change from a subsurface heat source. Most other features in the region are clearly related to topography, such as crater rims.

Forward model of Tb owing to solar illumination and topography

To improve on our ability to fit the Chang'e data with a unique CBVC heat flux source, we produce a forward model of expected microwave emission from the region without an anomalous geothermal heat source. We solve the heat diffusion equation for each location at the CBVC and nearby regions using a standard finite-difference approximation described in ref. 55 to model the lunar surface and subsurface temperature. We include effects of latitude, slope, slope azimuth, rock abundance, albedo and density profiles (characterized by the scale height of density or H parameter). We then use available slope, azimuth, density and albedo data to pick the appropriate temperature from a database of pre-run one-dimensional thermal models. This is not a full three-dimensional model in which facets exchange radiation as the authors used previously for studying polar regions[50,56–59], but more akin to the models presented in refs. 19,55.

We modelled temperatures based on local slope, x, and azimuth angle, γ (radians from north) computed from the gridded Lunar Reconnaissance Orbiter Camera (LROC) digital elevation model. In the temperature calculations, local time t (lunar hour 0 to 24) was adjusted based on the east–west component of the slope:

$$t' = t + \frac{12\ \mathrm{h}}{\pi}\tan^{-1}(x\sin\gamma)$$

and latitudes ϕ were adjusted based on the north–south component of the slope

$$\phi' = \phi + \frac{180°}{\pi}\tan^{-1}(x\cos\gamma)$$

The normal bolometric bond albedo quantifies the total solar radiation reflected by the lunar surface. The effective solar flux received by the lunar surface, F_e, can be expressed as: $F_e = (1 - A_\theta)F = (1 - (A_0 + 1 - \cos^{0.2752}\theta))S\cos\phi$, where $F = S\cos\phi$, θ is the solar incidence angle, S is the solar constant (1,361 W m^{-2}), ϕ is the latitude and A_0 is the normal bolometric bond albedo. In this study, we use a uniform best-fit albedo of 0.12 for the entire CBVC region. If anything, this will overestimate the solar heating contribution from the higher albedo CBVC feature—but we treat such effects as negligible.

As the thermal conductivity is density dependent, in the thermal model, the density of regolith at depth z is described by: $\rho(z) = \rho_d - (\rho_d - \rho_s)e^{-z/H}$, where ρ_s and ρ_d are the bounding densities at the surface and at depths much greater than H (ρ_s = 1,100 kg m^{-3} and ρ_d = 1,800 kg m^{-3}), respectively. The thermal conductivity of lunar regolith used in the thermal model is[60,61] $K(\rho, T) = K_c(\rho)[1 + \chi(T/350)^3]$, where χ is radiative conductivity parameter and $K_c(\rho)$ denotes the contact conductivity, linearly proportional to density[55,62] $K_c(\rho) = K_d - (K_d - K_s)\frac{\rho_d - \rho}{\rho_d - \rho_s}$, where K_s and K_d are the contact conductivity values at the surface and at depth, respectively.

Diviner rock abundance represents the fraction of a pixel covered by rocks larger than about 1 m in diameter. Fundamentally, rock has higher thermal inertia, so it is warmer at night. The contribution of infrared spectral radiance from rocks is given by

$$I_{rock}(\lambda, T_{rock}) = \varepsilon\frac{2hc^2}{\lambda^2}\left(e^{\frac{hc}{\lambda k T_{rock}}} - 1\right)^{-1}$$

where T_{rock} is the physical temperature of rocks, k is the Boltzmann constant, h is the Planck constant, c is the speed of light in the medium, ε is emissivity and λ is the wavelength. For each pixel with a rock fraction of f, the infrared spectral radiance is:

$$I = (1 - f)I_{regolith} + fI_{rock}$$

Then the physical temperature of each pixel is calculated from infrared spectral radiance. By applying the thermal model, each location's surface and subsurface temperature at the CBVC are calculated. Modelled brightness temperatures at four frequencies before convolution are shown in Extended Data Fig. 4.

The modelled Tb at four frequencies after convolution with our antenna models are shown in Extended Data Fig. 5. As these models do not include reflected radiation, areas such as Hayn Crater (northwest corner) are colder than in reality.

This forward model should bear a striking resemblance to Extended Data Fig. 3b if produced properly. This is illustrated in Extended Data Fig. 6, which shows the data in Extended Data Fig. 3b minus the model in Extended Data Fig. 5. Although some residuals exist, especially in the high-frequency models, most features in the CBVC region and about 61°-latitude band have been removed. These models are then used to produce Fig. 3. In that figure, we plot all data in these maps as a function of distance from the centre of the CBVC for convolutions using both the CE-1 and CE-2 orbital altitudes.

Extended Data Fig. 6 also illustrates the coincidence between the microwave Tb enhancement and the derived Lunar Prospector Th enhancement that led to the discovery of Compton–Belkovich[4]. Here we can see a clear spatial correlation between the heat flux anomaly and the Lunar Prospector Neutron Spectrometer (LPNS) Th, which is also illustrated in Extended Data Fig. 6e, which shows the inverse picture, with mapped pixon-reconstructed Th values[7] and contours

of 3-GHz ΔTb values. However, the directly derived Th concentration (about 7 ppm from the pixon reconstruction; Extended Data Fig. 6e) and even the remodelled surface Th concentration (according to ref. 7, is 14–26 ppm) is far too low of a radiogenic concentration to explain the approximately 180 mW m^{-2} heat flux required by our data.

Petrologic parameters

Noting that the surface Th concentrations are too low to explain the heat flux observed at the CBVC, we use geomorphology and lunar sample petrology to provide reasonable starting points for a heat source model.

The geomorphology of the CBVC is consistent with a volcanic caldera[9–12] that experienced piston-style collapse where the caldera floor faulted downwards in a fairly coherent block. This style of collapse forms above ellipsoidal, shallowly emplaced magma chambers[63] whose depth is less than the horizontal dimension[64]. Using the vents within the ring faults as a means to constrain the structural diameter of the caldera[12], the magma chamber is predicted to be about 13 km in diameter, probably being composed of smaller bodies, but having the net effect of a single heat source. Petrologic modelling of lunar granites constrains the upper magma emplacement depth to approximately 1 km (refs. 2,36). These parameters guide our preferred model, which assumes a simplified 2:1 ellipsoid 13 km in diameter (6.5-km thick) and a larger chamber below.

Three generalized granite families found in the Apollo returned sample collection can serve as reasonable estimates of the range of compositions that may exist on the Moon. As noted, the data presented here strongly support a scenario of partial melting and differentiation of KREEP-rich rocks. Indeed, although the deeper emplaced pluton is less enriched in radiogenic elements (about 60-ppm Th) than the upper, smaller pluton (about 132-ppm Th), this body still has Th concentrations much higher than the Apollo KREEP basalt samples. The enrichment from Apollo KREEP basalt concentrations to those of the modelled lower body are consistent with a partial melting and fractionation evolution that would achieve quartz monzodiorite to granite compositions. Thus, the lower body could form from extensive crystal fractionation of a KREEP basalt parent melt or as a result of partial melting of a KREEP-enriched monzogabbro or alkali gabbronorite lower crust. Likely, an ellipsoidal lower body simplifies a complex magmatic architecture (Extended Data Fig. 7).

The presence of a more evolved upper body suggests a multi-stage process wherein more evolved melts were extracted and segregated effectively from the lower magma chamber. Repeated extraction and further crystal fractionation of incompatible element-enriched silicic magmas would enable the formation of the upper magma chamber.

Details of finite-element forward models

Our end-member model of the 13-km-diameter upper pluton and 53-km lower pluton is not a unique solution, but is based on patterns seen in 528 example model runs. These steady-state models were produced using a Comsol Multiphysics finite-element heat conduction model to enable changes in density and properties as a function of depth. A steady state should be a safe assumption as the last eruptions of the CBVC were probably more than 3.5 billion years ago[65]. We approached the models with fixed parameters designed to minimize the size of both heat-producing bodies. These include:

(1) Foremost, we fixed the radiogenic heat production of both bodies. The upper pluton is limited to a heat production of 22 μW m^{-3}, consistent with the highest Th concentration granite found in the lunar sample collection, described here as type G_C. Although it may be true that the CBVC has an even higher concentration of radiogenic materials, we did not think it was reasonable to go beyond this measured value. The lower pluton was then fixed at 10.4 μW m^{-3} heat production, consistent with many moderate Th concentration granites, or type G_B.

(2) We forced the bodies to be as close to the surface as we felt plausible. The upper pluton was required to be at 1-km depth with the nominal. However, it is a somewhat arbitrary idea that this overburden is needed to have prevented the entire pluton from erupting 3.5 billion years ago. Moving the upper pluton closer to the surface would not increase heat flux markedly, mainly affecting the width of the peak well below MRM spatial resolution. We put the lower pluton as near to the surface as possible, so it was always just touching the bottom of the upper pluton. The lower pluton can be placed deeper, but this would require the lower pluton to be larger to produce the same surface heat flux and result in a spatially wider signal than seen.

(3) We forced the bodies to be ellipsoids, circular in the x–y plane, with a 2:1 aspect ratio. Again, this need not be the case, but this shape is a reasonable first-order model. We note that the horizontal dimensions of the bodies is constrained by the spatial pattern of the Tb anomaly, but there will be a trade-off between the best-fit vertical dimension (or aspect ratio) and assumed heat production.

We approached fitting the models to the data by running a suite of 176 diameter combinations of the two bodies. The upper body was allowed to vary between 10 km and 20 km in diameter, with limits set by the geometry of the surface topographic feature. We altered the lower body between 45 km and 60 km in diameter. These 176 models were run with three different density profiles and related thermal conductivity using the nominal density and conductivity profiles discussed in ref. 21. These assume an exponential density profile that increases density by a factor of e over a scale height of 1 km, 5 km and 10 km, consistent with GRAIL analysis[66]. The granites were given a thermal conductivity of 3.1 W m^{-1} K^{-1} (ref. 67). Here density of the granite bodies is set to 2,550 kg m^{-3}.

Extended Data Fig. 8a illustrates the suite of model fits run to fit the data following the three criteria listed above. These fits consider only the peak heat production with the plotted value representing the absolute value difference between the peak value in the data versus that of the model. These plots are for the 5-km e-folding model, but show similar results to other models (with best fits noted by an asterisk). The upper plots show the sum of the misfit between the peak in data and model for all four frequencies (for CE-1 and CE-2, respectively). The lower plots omit 37-GHz data from this fit, as it was most prone to the effects of surface temperature errors in the model.

All the plots show that a narrow avenue of pluton models minimizes the data–model differences. The minimum data–model difference for each crustal density model is plotted as a coloured asterisk, although many values along the minimum avenue are notably similar. The CE-2 data show a greater tendency towards smaller lower pluton models for large upper plutons owing to the fact its lower altitude shows less lateral smearing. On the basis of surface faulting, we again favour a smaller upper-pluton source, leading us towards this range, where all fits favour a roughly 53–56-km-wide lower pluton.

The plots in Extended Data Fig. 8b consider the best fit over the area ±15 km around the centre of CBVC, again for the 5-km e-folding model. Here we again sum the difference between data and model (differencing the lines from the data points in Fig. 3) over all frequencies, hoping to capture more information on the fit to the overall shape of the enhanced brightness temperature. These fits result in a slightly wider 'best-fit avenue' with minimum ranges for the lower pluton now centring around 52–55-km diameter. We do not plot minimum values here as they often ended up with a 20-km upper-body diameter, which is hard to reconcile with the surface caldera geometry. Although it is not unreasonable that a magma source body currently fills a different geometry than our chosen preferred 13-km-diameter, 6.5-km-thick upper pluton, we use that as a guide for our end-member 13-km/53-km upper-body/lower-body geometry.

Extended Data Fig. 9a,b illustrates the same model fits as in Extended Data Fig. 8b but with lower radiogenic concentrations in the upper

pluton. Although the 132-ppm sample was found in a small clast, it is not believed to represent a bulk radiogenic composition of a larger body on the Moon. As we do not have samples from the CBVC, it is speculative to suggest that such high concentrations exist there. Our end-member model used this high-Th G_C concentration assumption to minimize the heat production required from the lower body. This case resulted in an approximately 53-km best-fit diameter for this lower G_B concentration 'batholith'. In Extended Data Fig. 9a, we instead model the upper pluton as also G_B concentration; these fits result in a slightly larger lower body, approximately 56 km in diameter to aid in accounting for the extra heat flux. It is noted that the slightly higher values on the 'sum the difference' colour bars denotes that these fits are worse than the G_C assumption, probably pointing to a true upper-pluton concentration between G_B and G_C.

Extended Data Fig. 9b presents the extreme assumption, in which the upper pluton is devoid of radiogenic material. This would be the opposite 'end member', where all heat is coming from only a lower body, meaning the upper pluton (argued for by fault and caldera geometry) was fully evacuated. Here 'diameter of the upper pluton, D_U' could also be labelled as depth to the top of the lower body (where depth = 1 km + D_U/2). This requires larger lower bodies, but still under about 60 km (assuming G_B concentrations). We note, however, that the sum of the difference values is even larger, again pointing to the need for an upper body.

This is evidenced primarily from the need for high peaks TA values in the 19-GHz and 37-GHz channels. Without a highly concentrated central source, the high-frequency data should not have seen such high TA values. Assuming G_C as an upper limit for potential radiogenic concentrations on the Moon and this model, we conclude that a lower body (again assuming G_B concentrations and simple ellipsoidal shape) would therefore fall between about 53 km and 60 km in diameter between approximately 7.5 km and 11 km below the lunar surface. Although these models have wide range of assumptions, they provide a theoretical basis for the size of the system that must exist below the CBVC.

Gravity analyses

We took gravity data from the GRGM1200 gravity model[26]. Although the rank-minus-one constrained fields of that study provide improved correlations between the free air gravity and topography out to degree 1,200, we find that the resulting Bouguer gravity models show orbit parallel striping and other noise beyond degree 500 in this region, and so we limit our analyses to a degree 500 representation of the field. The gravity from topography was calculated[68] assuming a density of 2,500 kg m^{-3} (refs. 20,26) to calculate the Bouguer gravity.

As noted in the main text, the Bouguer gravity shows a distinctive positive gravity anomaly centred on the Th-rich spot and microwave Tb anomaly at the CBVC. However, this location also shows a positive topography mound, consistent with either a volcanic construct or upwarping of the crust above an intrusive body[9]. This raises the possibility that the observed positive Bouguer gravity anomaly at this location is simply a result of an incorrect density assumed in the terrain correction. We find that an assumed crustal density of 3,300 kg m^{-3} minimizes the CBVC's distinctive positive gravity anomaly. However, such a high density is at the high end of mare sample densities[27], is greater than regional mare surface densities as constrained by gravity[26] and is incompatible with the inferred silicic surface composition based on LRO data[9,11]. A silicic volcanic construct is more likely to have a density similar to the 2,500 kg m^{-3} value assumed for the surrounding lunar terrain[69].

Although the data show a distinctive positive gravity anomaly associated with the CBVC, it is superposed on the shoulder of the broader and larger-magnitude Bouguer gravity high associated with a large depression, consistent with either isostatically compensated thinned crust[20] or increased density and decreased porosity owing to a regional thermal anomaly[70]. Given the small magnitude of the CBVC anomaly relative to this broader gravity high, it is not possible to uniquely constrain the density structure of CBVC or directly invert the gravity for the subsurface density structure. Moreover, without added constraints on the geometry or density of the subsurface body, a unique solution is not possible.

Instead, we test whether the end-member pluton model is consistent with the observed gravity. We forward model the gravity arising from the pair of elliptical plutons, decomposing each pluton into a large number of rectangular prismatic elements[71], with a horizontal resolution of 1 km and vertical resolution of 0.5 km. In preliminary tests, we found that the shallow smaller body alone generates an overly sharp gravity anomaly inconsistent with the data. In comparison, the larger deeper body produces a gravity anomaly commensurate with the observations. The end-member pluton model indicates a higher Th concentration in the upper body, which would probably be associated with a more evolved and more silicic composition, and, thus a lower density. We impose the constraint that the upper body has a density contrast that is half that of the lower body, and then forward model the gravity arising from both plutons, which is then subtracted from the data.

We find that density contrasts for the lower body in the range of 60–120 kg m^{-3} generate models that, when subtracted from the data, largely remove the small-scale CBVC gravity anomaly, leaving behind a smoother shoulder of the broader Compton–Belkovich feature (Extended Data Fig. 10). Larger density contrasts leave behind a negative anomaly at the CBVC, whereas smaller density contrasts do not adequately remove the CBVC gravity anomaly. The density contrast of the lower body of 60–120 kg m^{-3} at a depth of 20.5 km would equate to a density of 2,940–3,000 kg m^{-3}, based on a linear density model for the farside highlands[26]. Assuming a low porosity, this density implies a somewhat less dense body than a typical mare[27], suggesting a more silicic composition. The upper body has a smaller density contrast relative to the less dense shallow crust, equivalent to a density of 2,470–2,500 kg m^{-3}. This low density is consistent with a more evolved granitic pluton, as inferred based on the microwave data.

We emphasize that the gravity models are not unique, given the variability of the field in this region and the inherent non-uniqueness of potential field data. However, given the preferred pluton structure and the observed gravity anomaly, the conclusion that the lower intrusive body must have a modest positive density contrast whereas the upper intrusive body must have a weaker density contrast is robust. The upper body thus requires a low absolute density given the vertical density structure of the crust derived from GRAIL gravity data. The resulting density models are consistent with the interpretations based on the microwave data.

Inclusion and ethics

The authors of this work have strived to provide an inclusive experience of all co-authors regardless of gender, career stage or nationality.

Data availability

The data used to make the figures in this paper are available at https://doi.org/10.5281/zenodo.7786749. The original Chang'e-1 and Chang'e-2 MRM data can be downloaded from http://moon.bao.ac.cn/index_en.jsp. Our group has also produced a readable global gridded data product of all available Chang'e-1 and Chang'e-2 data at https://zenodo.org/record/7790013. Source data are provided with this paper.

40. Zheng, Y. et al. First microwave map of the Moon with Chang'e-1 data: the role of local time in global imaging. *Icarus* **219**, 194–210 (2012).
41. Fa, W. & Jin, Y.-Q. A primary analysis of microwave brightness temperature of lunar surface from Chang-e 1 multi-channel radiometer observation and inversion of regolith layer thickness. *Icarus* **207**, 605–615 (2010).
42. Gong, X., Paige, D. A., Siegler, M. A. & Jin, Y.-Q. Inversion of dielectric properties of the lunar regolith media with temperature profiles using Chang'e microwave radiometer observations. *IEEE Trans. Geosci. Remote Sens.* **12**, 384–388 (2014).
43. Hu, G.-P., Chan, K. L., Zheng, Y.-C. & Xu, A.-A. A rock model for the cold and hot spots in the Chang'e microwave brightness temperature map. *IEEE Trans. Geosci. Remote Sens.* **56**, 5471–5480 (2018).

44. Wei, G., Byrne, S., Li, X. & Hu, G. Lunar surface and buried rock abundance retrieved from Chang'e-2 microwave and diviner data. *Planet. Sci. J.* **1**, 56 (2020).
45. Wei, G., Li, X. & Wang, S. Inversions of subsurface temperature and thermal diffusivity on the Moon based on high frequency of Chang'e-1 microwave radiometer data. *Icarus* **275**, 97–106 (2016).
46. Siegler, M. & Feng, J. Microwave remote sensing of lunar subsurface temperatures: reconciling Chang'e MRM and LRO diviner. In *Proc. Lunar and Planetary Science Conference* 1705 (Lunar and Planetary Institute, 2017).
47. Fang, T. & Fa, W. High frequency thermal emission from the lunar surface and near surface temperature of the Moon from Chang'e-2 microwave radiometer. *Icarus* **232**, 34–53 (2014).
48. Meng, Z. et al. Passive microwave probing mare basalts in mare Imbrium using CE-2 CELMS data. *IEEE J. Sel. Top. Appl. Earth Obs. Remote Sens.* **11**, 3097–3104 (2018).
49. Wei, G., Li, X. & Wang, S. Thermal behavior of regolith at cold traps on the Moon's south pole: revealed by Chang'e-2 microwave radiometer data. *Planet. Space Sci.* **122**, 101–109 (2016).
50. Feng, J. & Siegler, M. A. Reconciling the infrared and microwave observations of the lunar south pole: a study on subsurface temperature and regolith density. *J. Geophys. Res. Planets* **126**, e2020JE006623 (2021).
51. Ulaby, F. T., Moore, R. K. & Fung, A. K. *Microwave Remote Sensing: Active and Passive. Volume 2—Radar Remote Sensing and Surface Scattering and Emission Theory* (Artech House, 1982).
52. Ulaby, F. T., Moore, R. K. & Fung, A. K. *Microwave Remote Sensing: Active and Passive. Volume 3—From Theory to Applications* (Artech House, 1986).
53. Carrier, W. D. III, Olhoeft, G. R. & Mendell, W. *Physical Properties of the Lunar Surface: Lunar Sourcebook* 475–594 (Cambridge Univ. Press, 1991).
54. Wang, Z. et al. Calibration and brightness temperature algorithm of CE-1 Lunar Microwave Sounder (CELMS). *Sci. China Earth Sci.* **53**, 1392–1406 (2010).
55. Hayne, P. O. et al. Global regolith thermophysical properties of the Moon from the Diviner Lunar Radiometer Experiment. *J. Geophys. Res. Planets* **122**, 2371–2400 (2017).
56. Paige, D. A. et al. Thermal stability of volatiles in the north polar region of Mercury. *Science* **339**, 300–303 (2013).
57. Paige, D. A. et al. Diviner lunar radiometer observations of cold traps in the Moon's south polar region. *Science* **330**, 479–482 (2010).
58. Siegler, M., Paige, D., Williams, J. P. & Bills, B. Evolution of lunar polar ice stability. *Icarus* **255**, 78–87 (2015).
59. Siegler, M. A. et al. Lunar true polar wander inferred from polar hydrogen. *Nature* **531**, 480–484 (2016).
60. Mitchell, D. L. & De Pater, I. Microwave imaging of Mercury's thermal emission at wavelengths from 0.3 to 20.5 cm. *Icarus* **110**, 2–32 (1994).
61. Whipple, F. L. The theory of micro-meteorites: Part I. In an isothermal atmosphere. *Proc. Natl Acad. Sci. USA* **36**, 687–695 (1950).
62. Vasavada, A. R. et al. Lunar equatorial surface temperatures and regolith properties from the Diviner Lunar Radiometer Experiment. *J. Geophys. Res. Planets* **117**, E00H18 (2012).
63. Gudmundsson, A. Magma-chamber geometry, fluid transport, local stresses and rock behaviour during collapse caldera formation. *Dev. Volcanol.* **10**, 313–349 (2008).
64. Geyer, A., Folch, A. & Martí, J. Relationship between caldera collapse and magma chamber withdrawal: an experimental approach. *J. Volcanol. Geotherm. Res.* **157**, 375–386 (2006).
65. Shirley, K. A., Zanetti, M., Jolliff, B. L., van der Bogert, C. H. & Hiesinger, H. Crater size–frequency distribution measurements at the Compton–Belkovich Volcanic Complex. *Icarus* **273**, 214–223 (2016).
66. Besserer, J. et al. GRAIL gravity constraints on the vertical and lateral density structure of the lunar crust. *Geophys. Res. Lett.* **41**, 5771–5777 (2014).
67. Cho, W. J., Kwon, S. & Choi, J. W. The thermal conductivity for granite with various water contents. *Eng. Geol.* **107**, 167–171 (2009).
68. Wieczorek, M. A. & Phillips, R. J. Potential anomalies on a sphere: applications to the thickness of the lunar crust. *J. Geophys. Res.* **103**, 1715–1724 (1998).
69. Kiefer, W. S. et al. The bulk density of the small lunar volcanos Gruithuisen Delta and Hansteen Alpha: implications for volcano composition and petrogenesis. In Proc. *Lunar and Planetary Science Conference* Vol. 47, 1722 (Lunar and Planetary Institute, 2016).
70. Jansen, J. C. et al. The subsurface structure of the Compton–Belkovich thorium anomaly as revealed by GRAIL. In *Proc. Lunar and Planetary Science Conference* 1832, 2185 (Lunar and Planetary Institute, 2015).
71. Blakely, R. J. Approximating edges of source bodies from magnetic or gravity anomalies. *Geophysics* **51**, 1494–1498 (1986).

Acknowledgements This work was funded through Lunar Data Analysis Grant 80NSSC20K1430 and work related with the Lunar Reconnaissance Orbiter Diviner Lunar Radiometer.

Author contributions M.A.S.: primary writing, central ideas and concepts, figures and funding. J.F.: primary data processing, microwave modelling, writing, central ideas and data interpretation. K.L.-F.: petrologic model synthesis, writing and figure creation. J.C.A.-H.: gravity modelling, synthesis and writing. R.C.E.: petrologic model synthesis, writing and advised K.L.-F. M.S.C.: lead data product production (of global maps), science discussions, detailed review and editing. C.M.: aided in data product production (of global maps), science discussions, detailed review and editing. J.W.H.: science discussions, detailed review and editing. T.D.G.: science discussion, review and editing. M.N.W.: copy-editing and figure editing.

Competing interests The authors declare no competing interests.

Additional information

Supplementary information The online version contains supplementary material available at https://doi.org/10.1038/s41586-023-06183-5.

Correspondence and requests for materials should be addressed to Matthew A. Siegler or Jianqing Feng.

Peer review information *Nature* thanks David Lawrence and Sarah Valencia for their contribution to the peer review of this work. Peer reviewer reports are available.

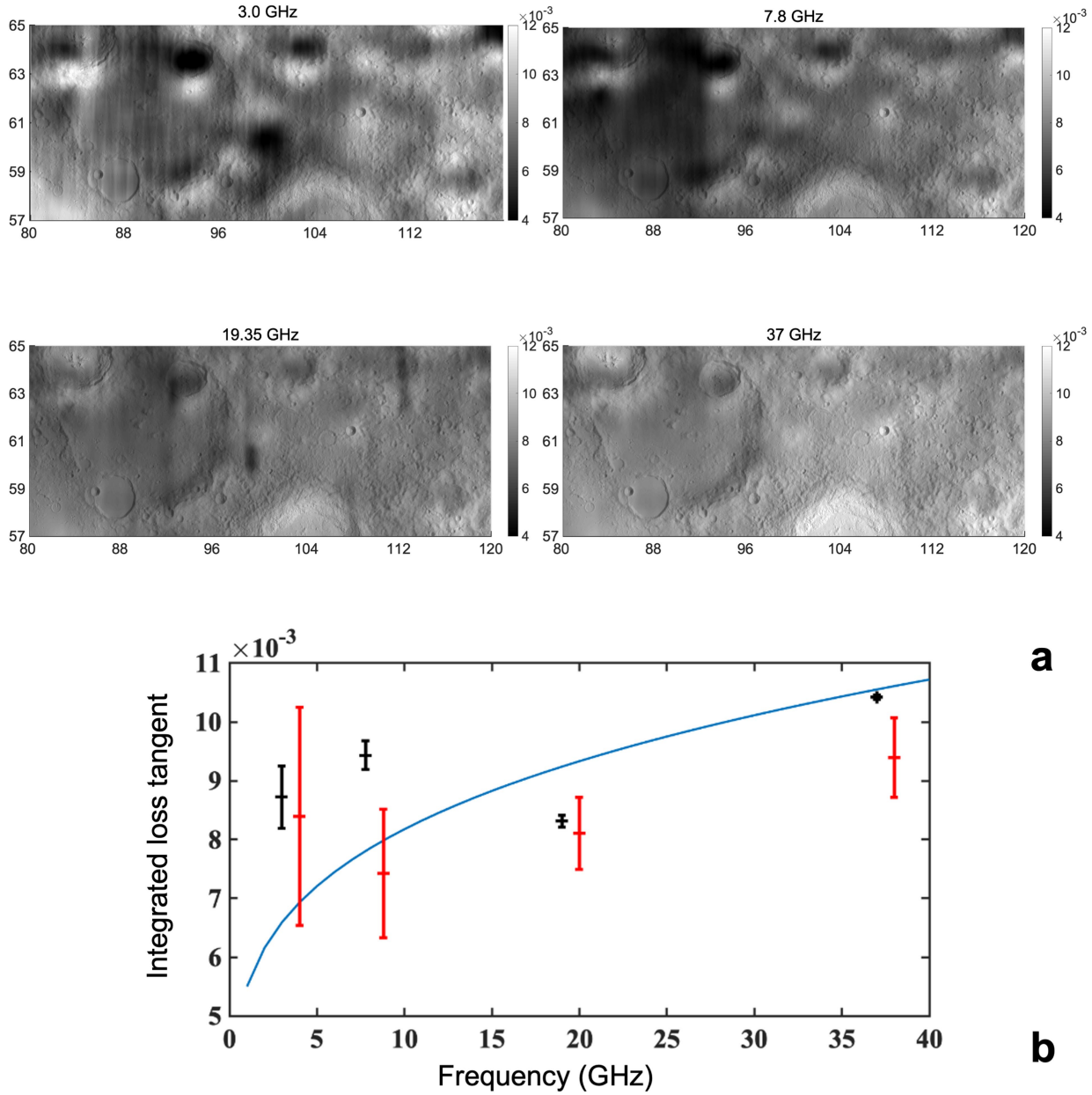

Extended Data Fig. 1 | Loss Tangent Derivation from Chang'e 2 data. (a) Integrated loss tangent for each of the four frequencies derived from Chang'e 2 microwave amplitudes and thermal model fits (as in[19]) (b) Integrated loss tangent as a function of frequency for (black) the areas within 1 degree of CBVC, (red) the entire maps in ED1, and (blue) the highlands terrain model from[19]. The blue line is used for our modeling of the CBVC heat flux.

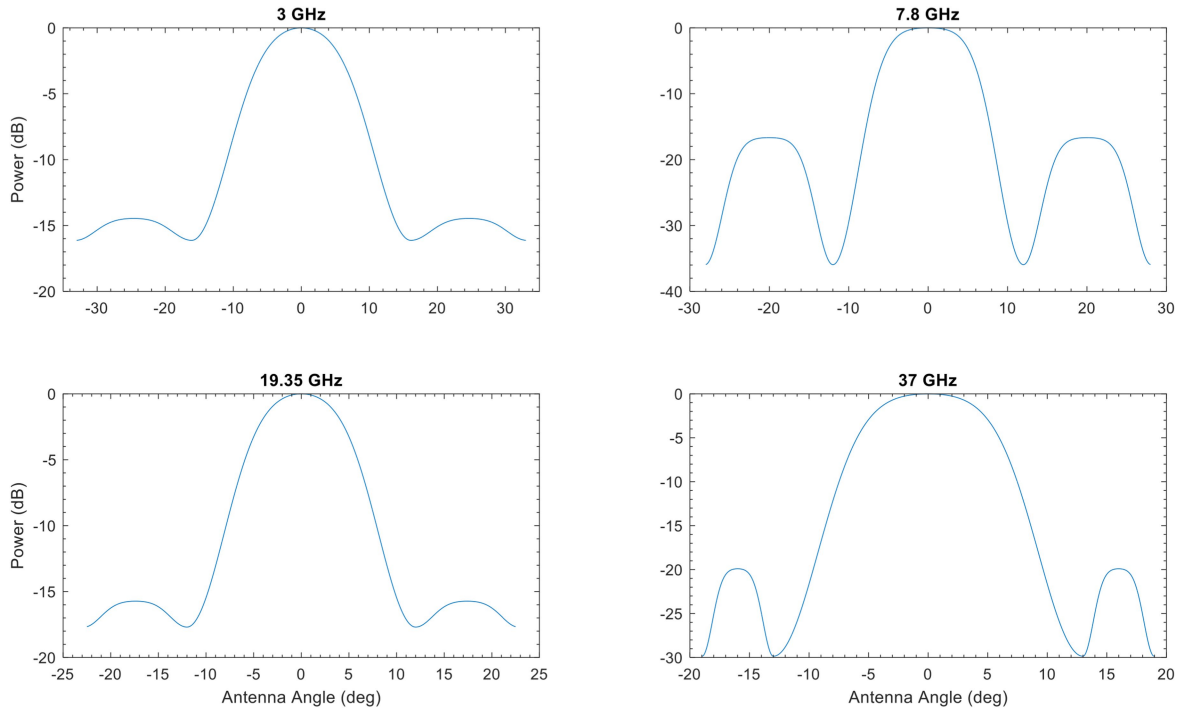

Extended Data Fig. 2 | Chang'e instrument antenna pattern models. Simulated antenna patterns for each of the four MRM frequencies. Here they are plotted in antenna angle, leading to different spatial footprints for the Chang'e 1 vs. 2 missions due to their 200 and 100 km altitudes.

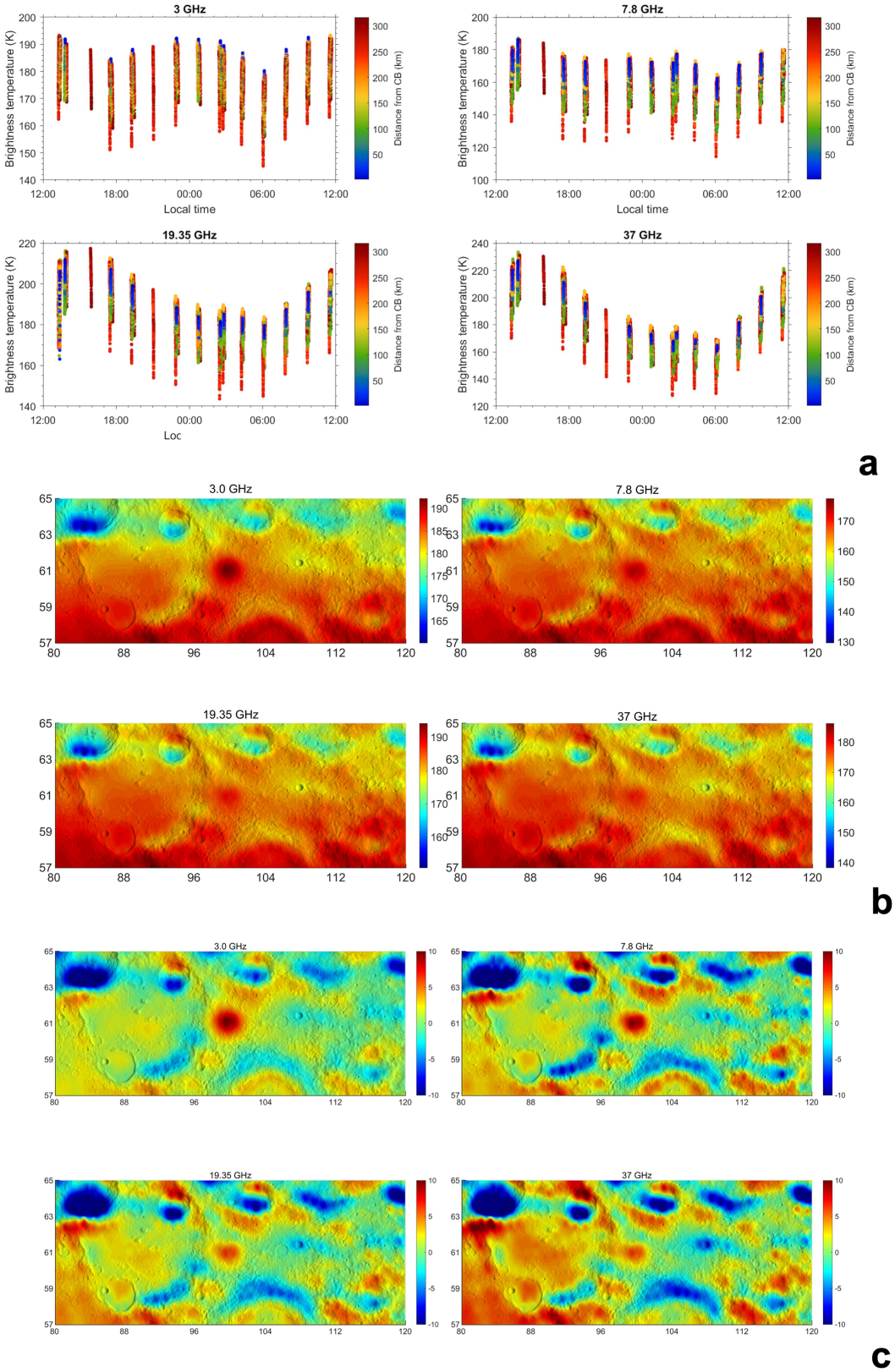

Extended Data Fig. 3 | Chang'e 2 antenna temperature data processing. (a) Antenna temperatures as a function of time of day and distance from CBVC, (b) Gridded noontime antenna temperature data from the Chang'e 2 MRM mission centered at Compton-Belkovich overlain on LROC WAC topography- units in K. Note the trend in temperatures with latitude. (c) Gridded Δ*TA* data from the Chang'e 2 MRM mission centered at Compton-Belkovich after latitude correction overlain on LROC WAC topography- units in K. The 3 GHz 3c figure is used in main text Fig. 1.

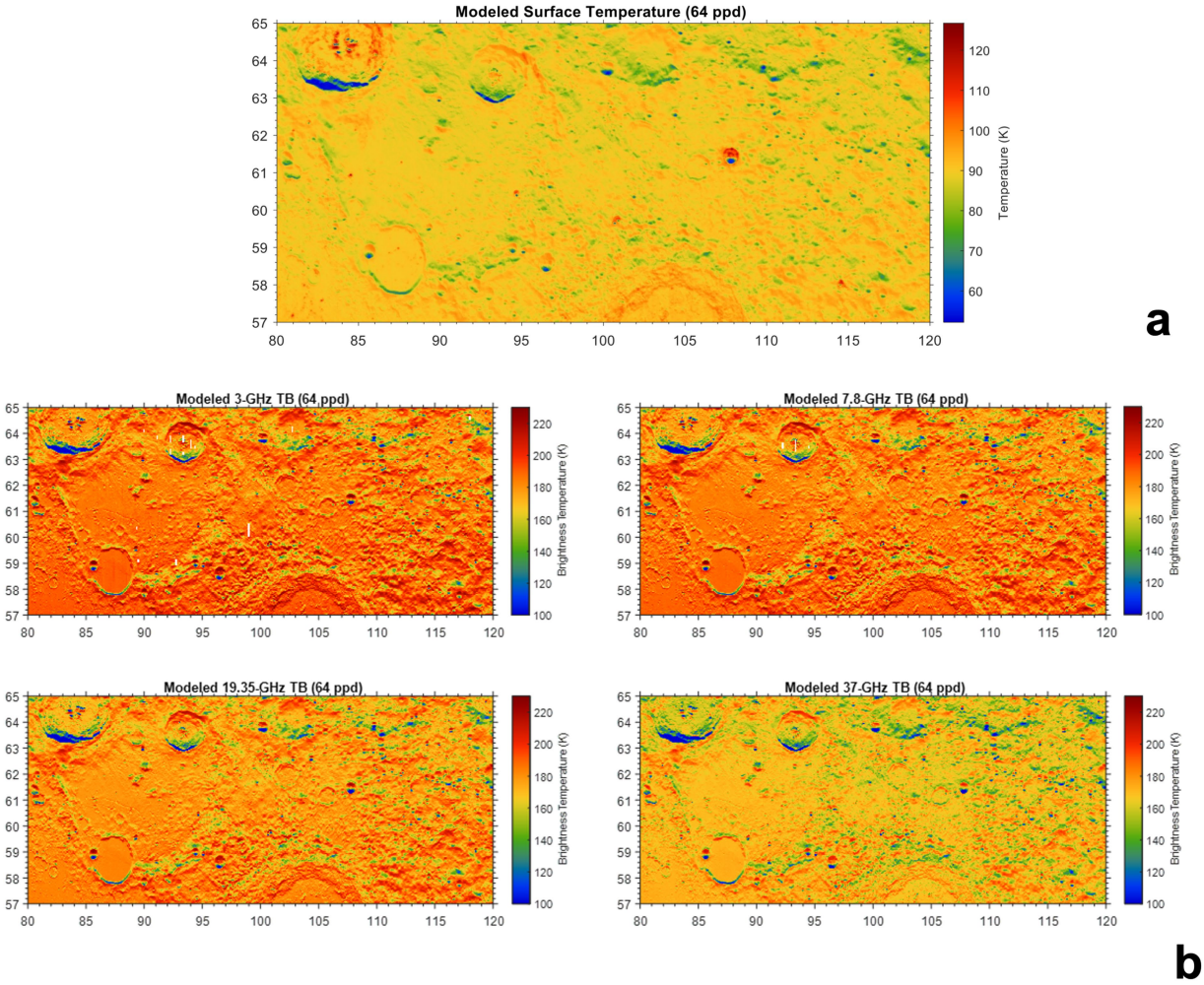

Extended Data Fig. 4 | Forward model based of brightness temperatures. (upper) Modeled surface temperature at night without a CBVC source. (lower) Full resolution modeled brightness temperature of four frequencies (again without a CBVC source) at night before convolution.

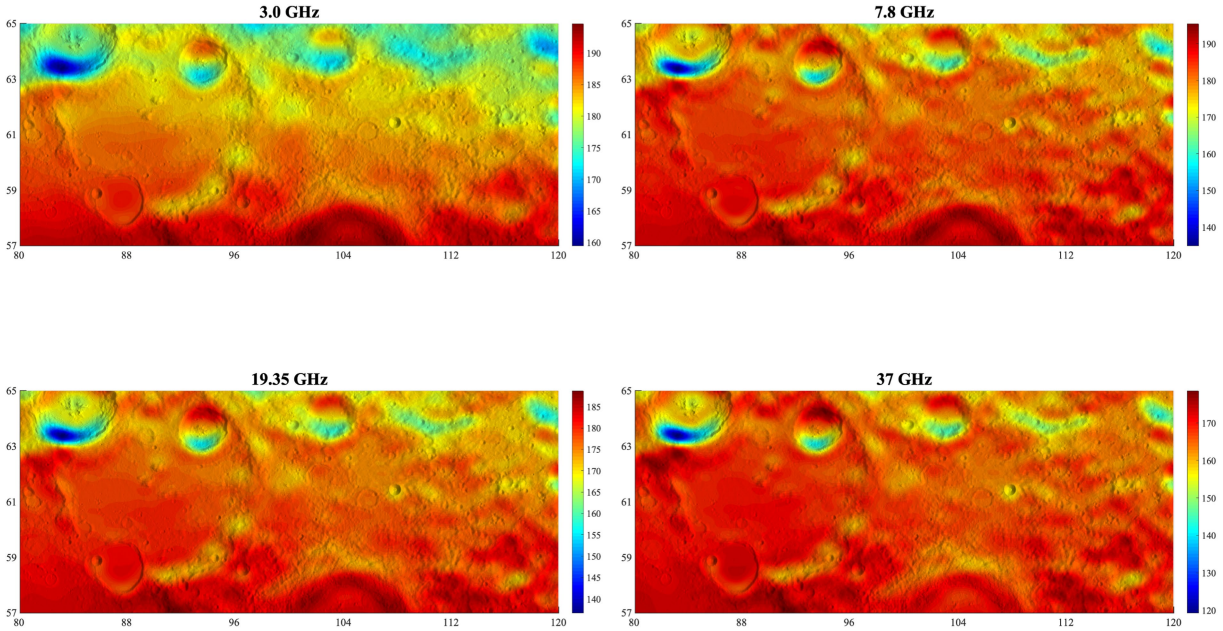

Extended Data Fig. 5 | Forward model of antenna temperatures, TA. The modeled antenna temperature (in the absence of a CBVC heat source) at four frequencies after convolution.

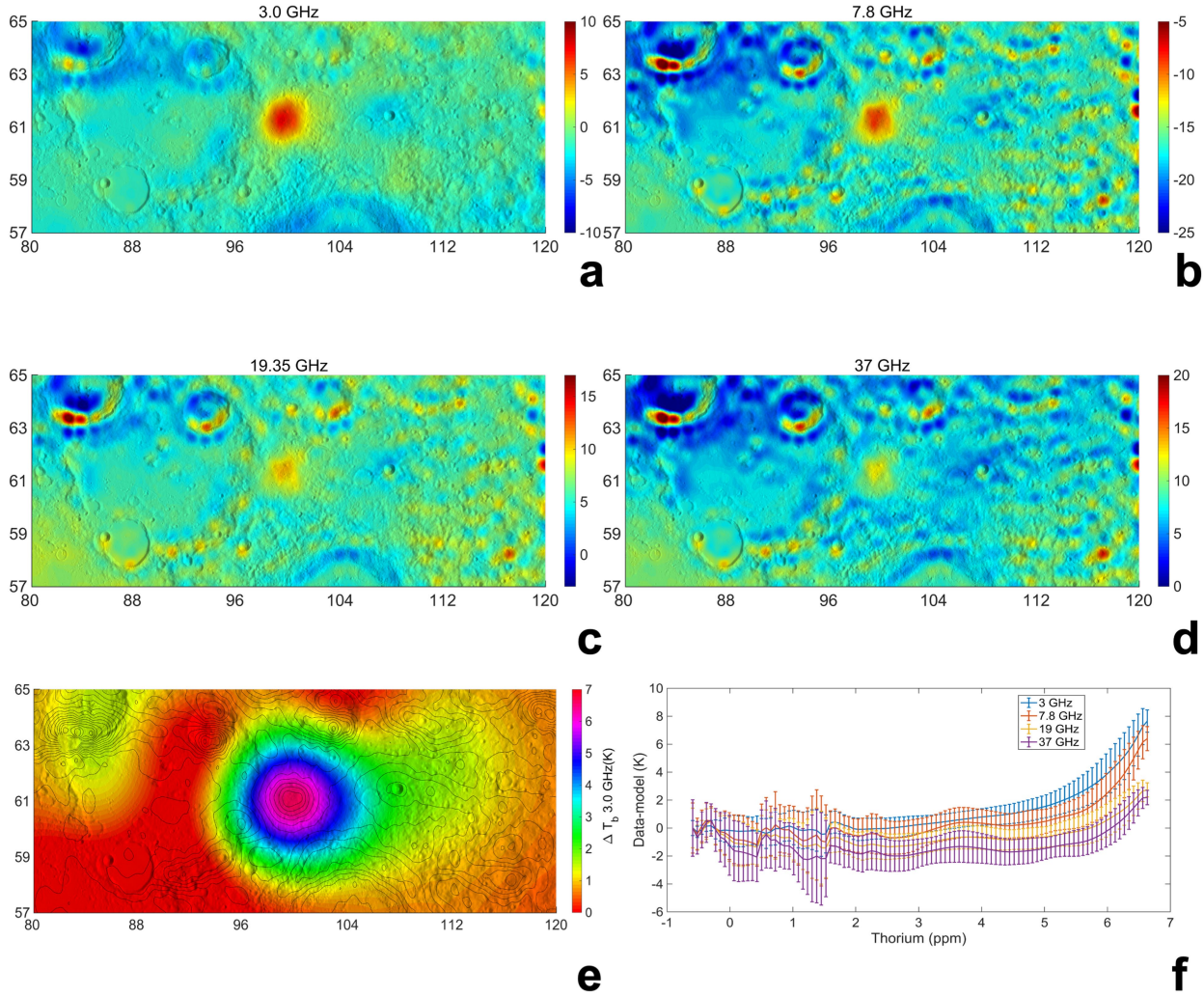

Extended Data Fig. 6 | Data/forward model differences. (a-d) The "data minus model" residual antenna temperature (units K) at four frequencies subtracted from the Chang'e 2 data. Contours map the LP-GRS Th enhancement (after Wilson et al.[7]), (e) The pixon-reconstructed LP-GRS Th concentrations with contours of CE-2 3 GHz data- model values. (f) CE-2 data minus model residual antenna temperature at four frequencies as a function of surface measured Th.

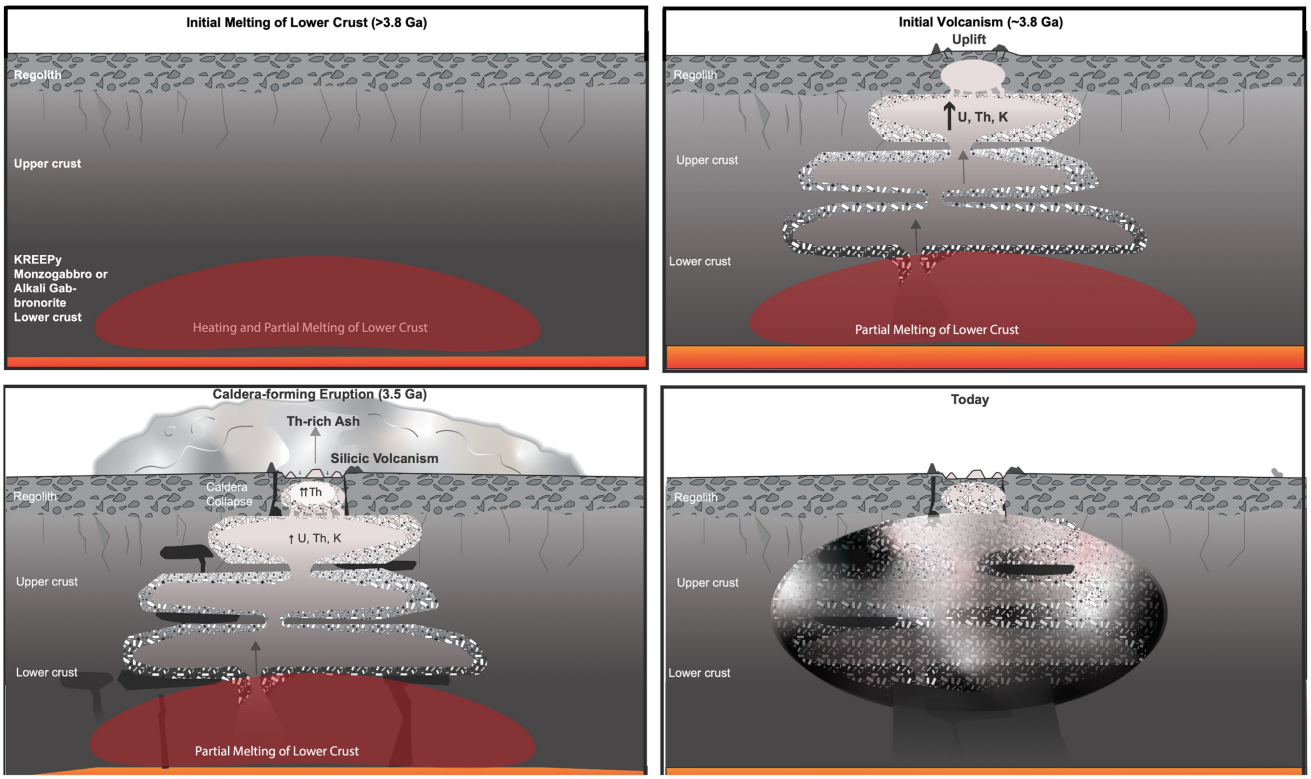

Extended Data Fig. 7 | Possible evolution of the CBVC subsurface system. The resolution of the gravity and heat flow models is insufficient to inform internal variations in a body that must have formed from a complex system of magma chambers. This figure is one example of a system that could be represented by the Compton Belkovich batholith model and how that system could develop over time.

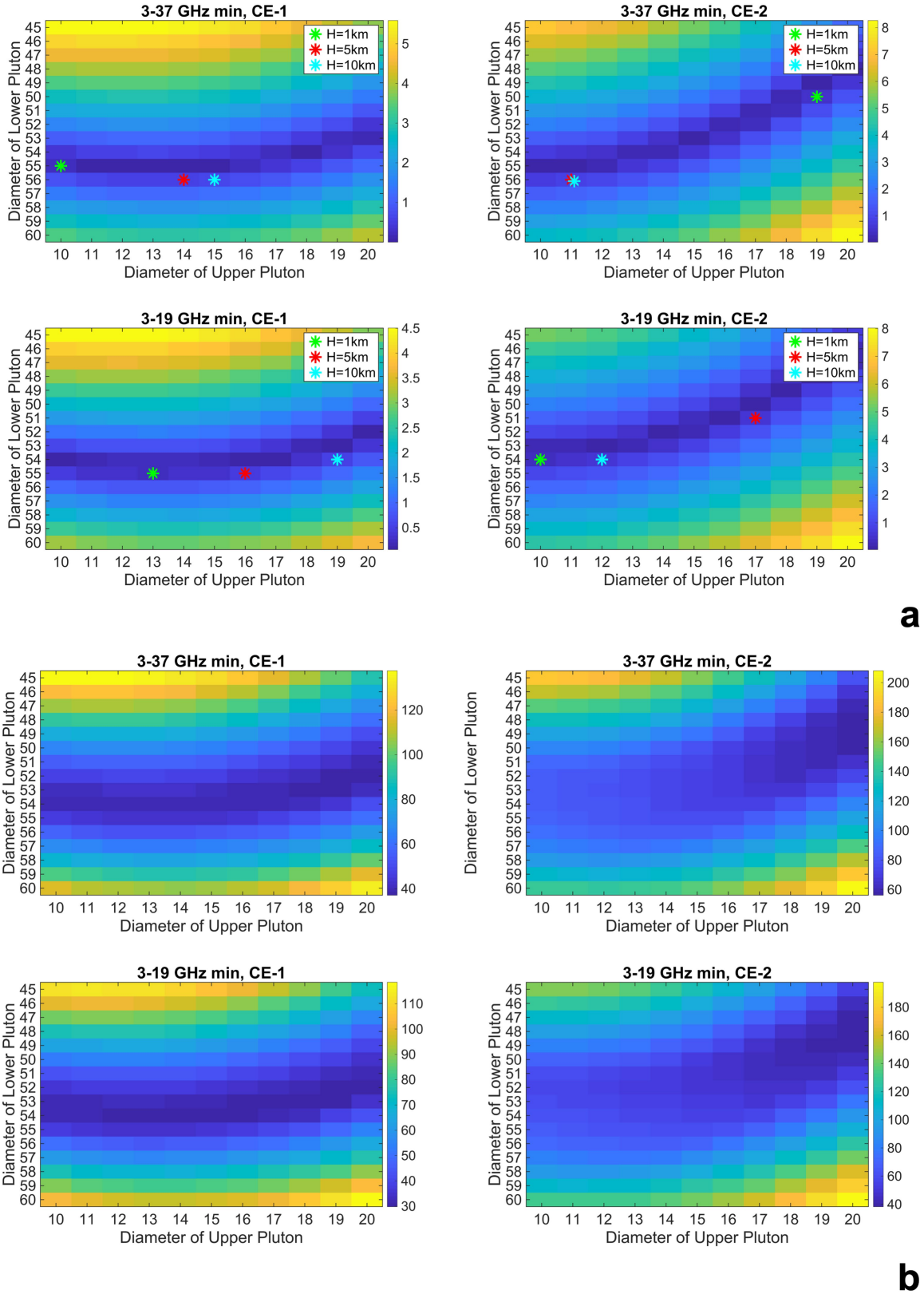

Extended Data Fig. 8 | Model differences as a function of pluton geometry. (a) Absolute data-model differences in peak *TA* for the 5 km e-folding density crustal model for various pluton diameters. Stars show minima for different crustal density models. (b) Absolute data-model differences in peak *TA* over the area within 15 km of the center of CBVC for the 5 km e-folding density crustal model for various pluton diameters.

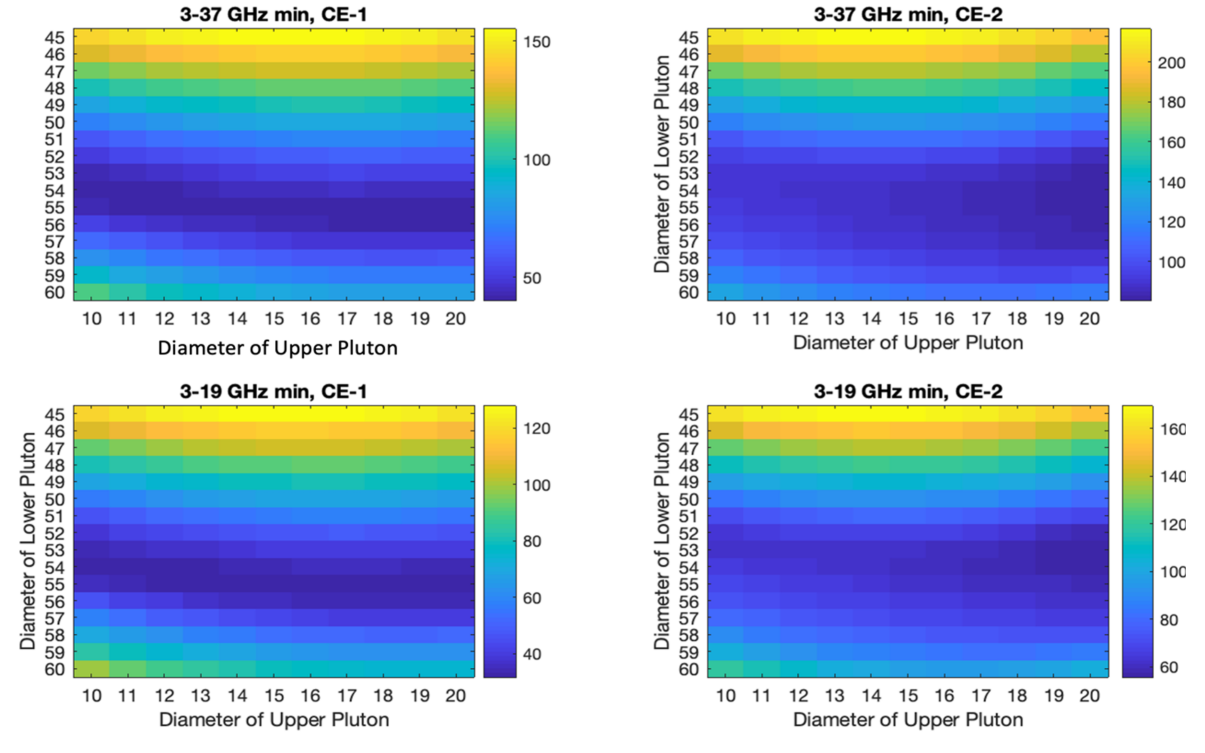

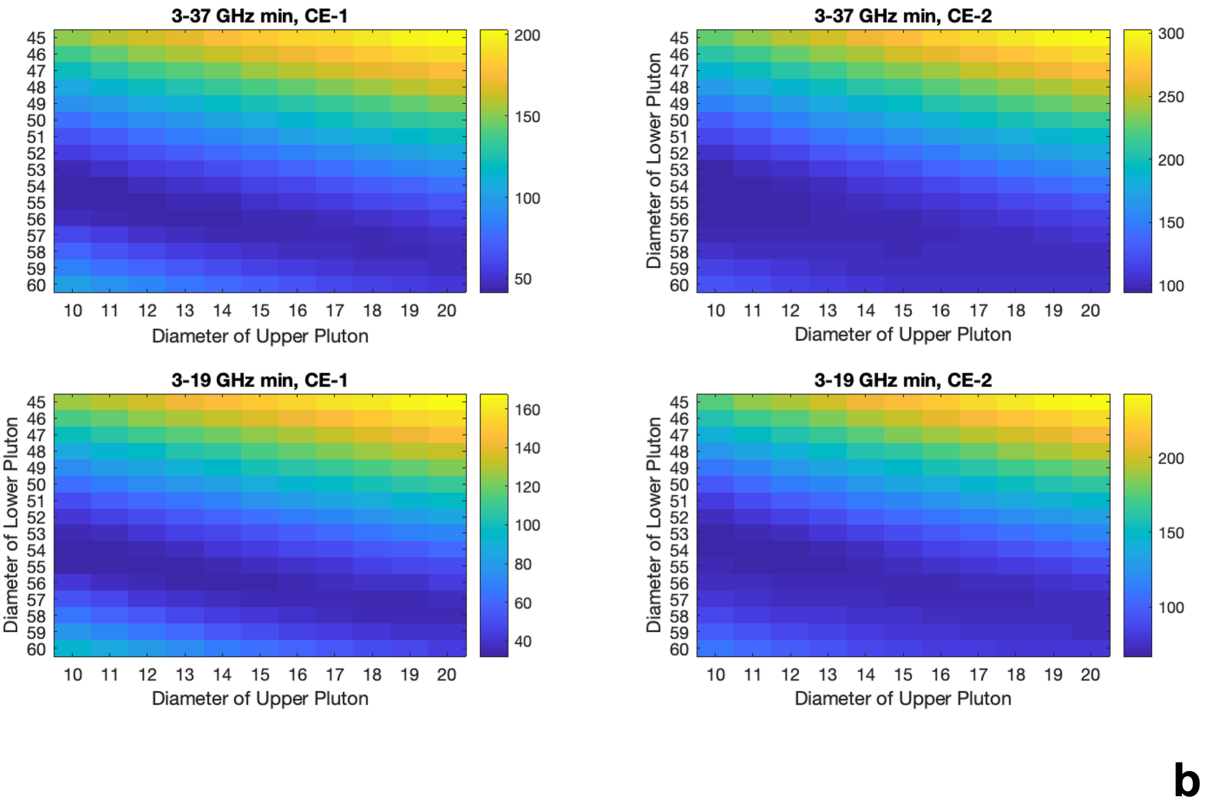

Extended Data Fig. 9 | Model differences as a function of pluton geometry examining sensitivity to heat production of upper pluton. (a) same as 8b, but for both the upper and lower pluton at 69.7 ppm Th. (b) 8b and 9a, but with no heat production from upper pluton and lower Pluton at 69.7 ppm Th, showing that most of the heat observed heat is coming from the lower magmatic system.

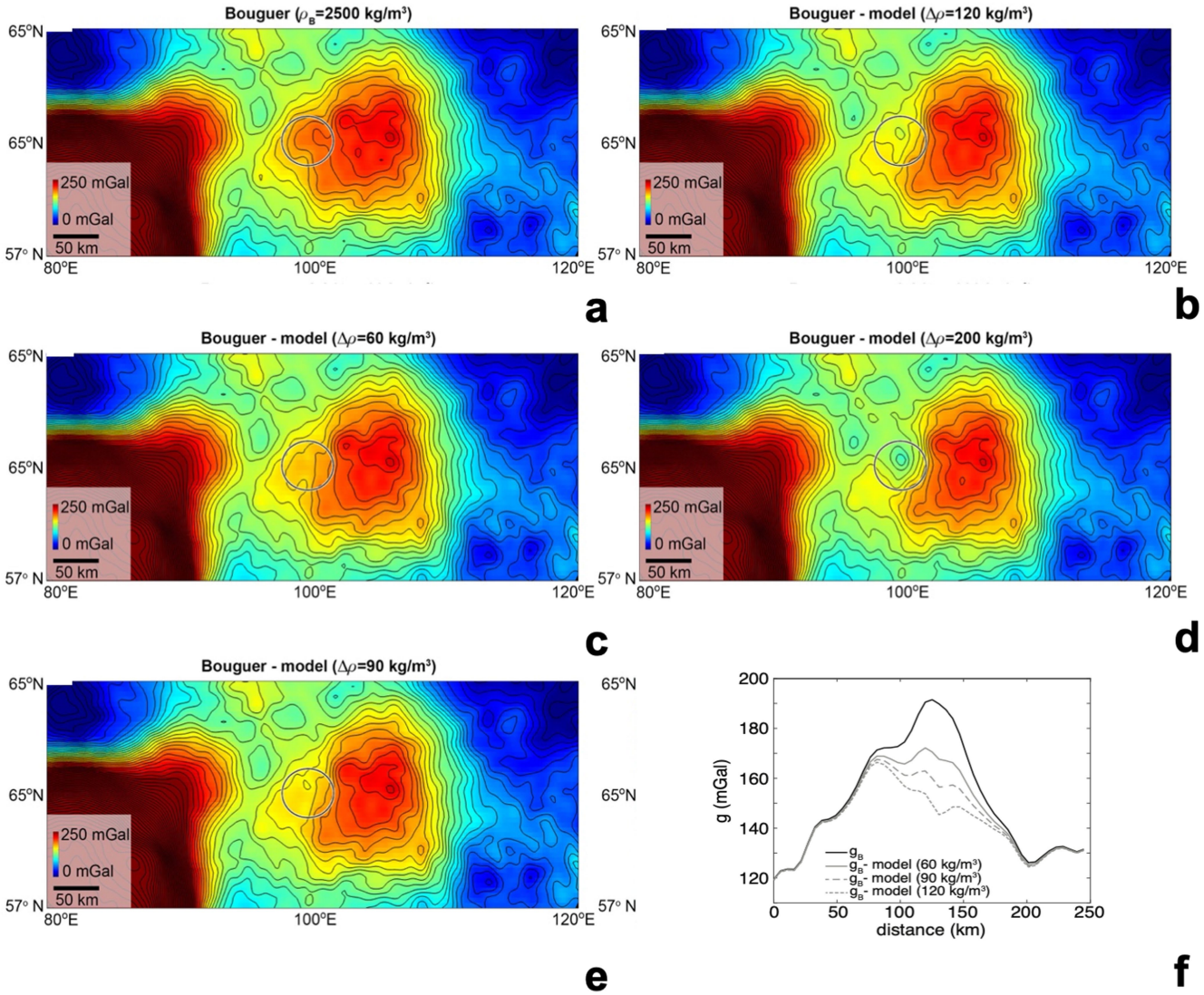

Extended Data Fig. 10 | Gravity models and GRAIL data for the CBVC. Observed Bouguer gravity data and model corrected Bouguer gravity. Bouguer gravity for an assumed crustal density of (a) 2500 kg/m^3, with corrections for the modeled density assuming lower intrusion densities of (b) 60 kg/m^3, (c) 90 kg/m^3, (d) 120 kg/m^3, and (e) 200 kg/m^3 and (f) North-south profiles of the observed and model corrected Bouguer gravity for assumed density contrasts of 60–120 kg/m^3.